CIRCUMSTELLAR ENVELOPE STRUCTURE OF LATE-TYPE STARS

P. F. BOWERS,[1] K. J. JOHNSTON, AND J. H. SPENCER
E. O. Hulburt Center for Space Research, Naval Research Laboratory

ABSTRACT

The arcsecond structure of OH maser clouds surrounding 20 Mira variables and late-type supergiants has been measured using the Very Large Array in a spectral line mode at 1612 MHz. Angular radii of the maser clouds range from $< 0\rlap{.}''5$ to $4''$ and have been combined with phase lag measurements of the shell size (if available) to estimate distances for some of the stars. The outer radii range from 100 AU to 10^4 AU, and we estimate a ratio of outer to inner radii $\lesssim 4$ for the maser regions. We confirm our previously discovered correlation between the mass loss rate and the outer radius of the maser region and use it to determine the mass loss rates for eight stars. Mass loss rates range from 1 to 50×10^{-6} $M_\odot$ yr^{-1} for the Mira-type OH/IR stars and are $\gtrsim 10^{-4}$ $M_\odot$ yr^{-1} for the supergiant stars VY CMa, IRC +10420, and NML Cyg.

Although one star (VY CMa) displays a complex, expanding disklike geometry, the circumstellar envelopes of the remaining stars are predominantly spherical. However, the observed OH distributions can deviate considerably from that predicted by the idealized expanding, spherical shell model because of density clumping ($\sim 10^{15}$–10^{16} cm) and streaming motions which can range up to 7 km s^{-1}. The influence of the interstellar ultraviolet radiation field on these quantities can be significant.

Our results suggest that spherical envelopes are commonly associated with evolved stars and indicate a mass loss mechanism such as a radiation-driven or shock-driven wind. In contrast, evolved stars with nonspherical envelopes are spatially rare. Examples are bipolar nebulae, nonspherical planetary nebulae, and carbon stars. We suggest that the circumstellar geometry and mass loss for these latter systems are influenced by close binary companions. The evolutionary link among these objects is discussed.

Subject headings: interferometry — masers — stars: circumstellar shells — stars: late-type — stars: long-period variables — stars: mass loss

I. INTRODUCTION

Late-type, oxygen-rich Mira variables and supergiant stars often undergo high mass loss ($\gtrsim 10^{-6}$ $M_\odot$ yr^{-1}) and various molecular species (OH, H_2O, SiO, CO) can be found in their extensive envelopes. The OH maser at 1612 MHz is particularly useful to ascertain properties of the outer envelope since it is commonly associated with these stars (> 200 type II OH/IR stars are known), has a characteristic double-peaked velocity signature believed to be formed by gas expanding at a nearly constant velocity in a spherical shell, and has high brightness temperatures ($\gtrsim 10^9$ K) which allow the associated stars to be detected at large distances from the Earth, unhindered by the effects of interstellar absorption.

Models of the maser line profiles provide two predictions for an expanding, spherical shell: (1) The low and high velocity peaks are due, respectively, to blue- and redshifted gas relative to the star and are coincident at the stellar position. (2) Gas at intermediate velocities is distributed in a circular ring centered on the stellar position; the size of the ring increases as the velocity approaches the stellar radial velocity defined by the midpoint of the peaks (Kwok 1976; Elitzur, Goldreich, and Scoville 1976; Olnon 1977; Reid *et al.* 1977; Morris and Bowers 1980).

High angular resolution observations obtained with very long baseline interferometric techniques (VLBI) show that maser features from these stars occur as seemingly random distributions of spots with diameters ranging from $< 0\rlap{.}''05$ to $> 0\rlap{.}''1$. These data do not demonstrate clearly the predictions of the model but indicate that much of the emission arises from regions $\gtrsim$ a few tenths of an arcsecond and is not detectable with baselines $\gtrsim 100$ km (Reid *et al.* 1977; Bowers *et al.* 1980).

Evidence directly supporting an expanding, spherical shell model has been obtained with the advent of intermediate resolution ($\sim 1''$), spectral line capabilities

(Bowers, Johnston, and Spencer 1981, hereafter BJS; Baud 1981; Reid, Moran, and Johnston 1981; Norris, Diamond, and Booth 1982). These data indicate positional coincidence to within 0″.3 for the low and high velocity components and a size dependence with velocity which support, to first order, the simple model.

BJS presented initial results of VLA observations at 1612 MHz for 20 OH/IR stars; conclusions were based on separate integration over the total velocity extent of the low and high velocity emission features of each source. A discussion of four of these stars (IRC +10011, R Aql, RR Aql, and NML Cyg) for which VLA observations of H_2O and OH (1665/1667 MHz) also were obtained is presented by Spencer, Bowers, and Johnston (1983, hereafter SBJ). VLA data at 1612 and 1667 MHz for the peculiar supergiant star IRC +10420 also are discussed elsewhere (Bowers 1983). In the present paper we present the data for the remaining stars, compare the extent and relative positions of individual spectral features at 1612 MHz to current theoretical models, and discuss the implications for mass loss mechanisms and the evolutionary fate of these stars.

II. OBSERVATIONS AND DATA REDUCTION

The interferometric observations were conducted during 22–23 November 1980 by using the NRAO[2] Very Large Array with nine antennas in the A configuration. Three antennas were used on each arm, giving baseline lengths ranging from 0.9 km to 30 km. The array was used in a spectral line mode with 128 channels of the circulating correlator receiving right circular polarization and with the bandpass centered at the average radial velocity of each double-peaked profile. The channel-to-channel velocity separation was 0.57 km s^{-1} (3.1 kHz), the velocity resolution after Hanning smoothing was 1.14 km s^{-1} (6.1 kHz), and the effective total velocity coverage was 73 km s^{-1} (0.39 MHz) at a rest frequency of 1612.231 MHz.

Each star was observed for about 20 minutes at each of three or four hour angles to provide a distribution of observations in the uv plane. Nearby calibrators were observed approximately every 30 minutes. The data were calibrated with the standard VLA reduction package which uses the phases and amplitudes of the calibrator sources to correct for instrumental effects. We estimate a total error of about ±0″.3 for absolute positions and ±0″.1 for relative positions of spectral features.

A 1 hr observation of 3C 286 (1328+307) was also obtained. The data displayed no significant phase or amplitude variations across the bandpass, so no band-

pass corrections were applied. The flux density scale was set from the adopted flux density for 3C 286 of 13.83 Jy (1 Jy = 10^{-26} W m^{-2} Hz^{-1}) at 1612 MHz (cf. Baars et al. 1977).

The calibrated visibility data for each source were scalar averaged to determine those channels with detectable (> 0.5 Jy) emission. Maps were made of every alternate (independent) spectral channel where emission was detected, using uniform weighting in the uv plane. The maps were then cleaned with the standard algorithm of Högbom (1974) and restored with a two-dimensional Gaussian beam whose shape depended on the synthesized beam resulting from the uv coverage. The dynamic range of the maps varies from 10:1 to 20:1, depending on the uv coverage.

Single-dish observations of these stars were obtained by P. F. B. during 1981 January 21 as part of a larger program to monitor the flux density of ~100 type II OH/IR stars (P. F. Bowers, unpublished). The data were obtained with the NRAO 140 foot (43 m) radio telescope at Green Bank, West Virginia. Two quadrants of the 1024 channel autocorrelator were used in a frequency-switched mode as independent 256 channel autocorrelators which received orthogonal linear polarizations. The bandwidth of each autocorrelator was 625 kHz, giving a resolution of 0.55 km s^{-1} (2.95 kHz).

The signals were combined to produce the total intensity profiles shown in this paper. The flux density scale was determined from observations of 3C 123 and 3C 218 with adopted fluxes and spectral indices given by Genzel, Pauliny-Toth, and Witzel (1976). Fluxes of the Green Bank profiles subsequently were compared to the fluxes established for the VLA profiles and maps to check the flux density scale in the latter case and to ensure that all the OH flux density is contained in the maps. For the 20 stars in this program, the ratio of VLA to Green Bank flux is 0.95 ± 0.23. It is unlikely that the maser clouds have extended, low-level components with sizes much greater than those derived in this paper.

III. RESULTS

a) Positions of the Stars

The position of the central star is not given directly by observations of OH masers but must be inferred in the context of a model. The expanding, spherical shell model predicts that the low and high velocity peak emission should be precisely coincident at the position of the star. However, careful inspection of the data suggests that the positions of the extreme velocity features at the outer edges of the profile are a better indicator of the stellar position if the signal-to-noise ratio is sufficiently large (≳1 Jy per beam for these observations). The best support for this statement is based on the strong source OH 26.5+0.6 which appears

---

[2] The National Radio Astronomy Observatory is operated by Associated Universities, Incorporated under contract to the National Science Foundation.

TABLE 1

VLA Positions of OH/IR Stars Precessed from Epoch 1980.9

Star	α(1950)	δ(1950)	Δ_α (arcsec)	Δ_δ (arcsec)	Comments
IRC +10011	$01^h03^m48^s09$	$+12°19'51''4$	−0.2	−0.4	1, 2
OH 127.8−0.0 ...	01 30 27.63	+62 11 31.2	≤ 0.1	≤ 0.1	
OH 138.0+7.3 ...	03 20 41.48	+65 21 32.8	≤ 0.1	≤ 0.1	
OH 141.7+3.5 ...	03 29 23.65	+60 10 04.4	≤ 0.1	≤ 0.1	
IRC +50137	05 07 19.68	+52 48 53.9	≤ 0.1	+0.3	
U Ori............	05 52 50.92	+20 10 06.0	−0.2	≤ 0.1	3
IRC +40156	06 29 45.03	+40 45 08.2	...	...	4
VY CMa	07 20 54.74	−25 40 12.4	−0.4	−0.4	5
IRC −20197	09 42 56.55	−21 47 54.4	≤ 0.1	+0.3	
WX Ser..........	15 25 31.98	+19 44 13.0	≤ 0.1	≤ 0.1	
OH 17.7−2.0	18 27 39.77	−14 31 03.9	≤ 0.1	≤ 0.1	
OH 26.5+0.6	18 34 52.47	−05 26 37.1	≤ 0.1	+0.2	2
OH 25.1−0.4	18 35 33.36	−07 12 35.2	≤ 0.1	≤ 0.1	6
OH 32.8−0.3	18 49 48.16	−00 17 53.5	...	...	7
OH 39.7+1.5	18 56 03.88	+06 38 49.8	≤ 0.1	≤ 0.1	
OH 39.9+0.0	19 01 42.90	+06 08 44.2	≤ 0.1	≤ 0.1	8
R Aql............	19 03 57.67	+08 09 07.7	≤ 0.1	≤ 0.1	1, 3
IRC +10420	19 24 26.74	+11 15 10.9	...	...	9, 10
RR Aql..........	19 55 00.30	−02 01 17.1	+0.2	+0.2	1, 2
NML Cyg	20 44 33.84	+39 55 57.1	−1.0	+0.2	1, 2

Comments.—(1) See map of SBJ. (2) Position is mean of extreme velocity features; values of Δ_α and Δ_δ are differences between low and high peak velocities. (3) Measured position has been precessed from epoch 1980.9 and includes no correction for the known proper motion of this star. (4) Only one spectral feature detected ($V = -27.9$ km s^{-1}). (5) Values are mean position and difference for the velocity ranges -13 to -5 km s^{-1} and $+47$ to $+55$ km s^{-1}. (6) Formerly OH 25.1−0.3. (7) Position given for low velocity peak feature at $+45.3$ km s^{-1}. (8) Formerly OH 39.9−0.0. (9) Position is mean of extreme velocity features; there is no well-defined peak in the profile of the high velocity emission. (10) See map of Bowers 1983.

to have a predominantly spherical shell (see the Appendix). The extreme velocity features are coincident, but the peak features are separated by 0″.2 with a mean δ(1950) = $-05°26'37''.4$ which differs by 0″.3 from the mean of the extreme velocity features.

Table 1 gives the derived position for each of the 20 stars and the differences Δ_α and Δ_δ between the positions of the low and high velocity peak features. The mean position of the peaks is listed if the source is weak or if this position is within 0″.1 of the mean of the extreme velocity features. If there is a positional discrepancy and the maximum map flux is >1 Jy per beam for the extreme velocity features, their mean position is listed. These cases are noted in Table 1. Finally, for two stars the positions are derived from only one peak velocity component. For IRC +40156, only one feature was detected; for OH 32.8−0.3, the structure of the two peak features is significantly different (see the Appendix.)

The positions in Table 1 agree to within 0″.3 with those derived by BJS from the stronger integrated velocity range. Comparison to other VLA estimates (Reid, Moran, and Johnston 1981; Baud 1981) and to optical estimates (see SBJ) indicate agreement to within about ±1″.

b) Radial and Expansion Velocities

The systemic radial velocity V_0 and circumstellar expansion velocity V_e determined from the Green Bank data are listed in Table 2. V_0 is the mean velocity of the outer peak features and usually agrees to within 0.6 km s^{-1} (rms) with the value V_0^w which is the mean of the total velocity range. For some stars our VLA data provide additional estimates of V_0 from (1) parabolic fits of the radius-velocity relation in § IIIc, and (2) the presence of front-back symmetric structure which occurs at velocities equidistant from the stellar velocity (Appendix; SBJ). These independent estimates confirm that the mean velocity of the outer peaks is a good (±1 km s^{-1}) indicator of the stellar radial velocity.

Comparison to published values of V_0 derived from the mean velocity of the thermal SiO ($J = 2-1$, $v = 0$) transition shows agreement to within a few km s^{-1} for cases where both species are detected (see Notes to Table 2). Uncertainties in the values of V_0 (SiO) tend to be larger than those for V_0 (OH) because the thermal profiles are broad and often have low signal-to-noise ratios, whereas the OH profiles have relatively narrow, well-defined peaks. The use of OH (1612) emission to

TABLE 2

STELLAR RADIAL VELOCITIES (V_0) AND CIRCUMSTELLAR EXPANSION
VELOCITIES (V_e) DETERMINED FROM 1612 MHz PROFILES

Star	V_0 (km s^{-1})	$(V_0^W - V_0)$ (km s^{-1})	V_e (km s^{-1})	$(V_e - V_e^P)$ (km s^{-1})	Notes
IRC +10011	+8.7	+0.1	19.3	0.9	1
OH 127.8−0.0 ...	−55.0	0.0	12.7	1.4	
OH 138.0+7.3 ...	−37.8	0.0	10.4	0.8	
OH 141.7+3.5 ...	−57.4	0.0	12.7	0.7	
IRC +50137	+2.9	+0.1	17.7	1.0	
U Ori	−44.4	0.0	3.6	0.6	
IRC +40156	−16.1	0.0	12.5	0.6	
VY CMa	+21.1	+1.9	38.9	6.9	2, 3
IRC −20197	+39.4	0.0	12.8	0.6	
WX Ser	+6.4	−0.2	8.0	0.7	
OH 17.7−2.0	+60.8	+0.4	14.3	2.3	
OH 26.5+0.6	+27.0	0.0	15.4	1.3	
OH 25.1−0.4	+142.7	+0.2	13.2	0.8	
OH 32.8−0.3	+60.9	−0.5	17.7	2.3	
OH 39.7+1.5	+19.8	+0.2	17.7	1.3	
OH 39.9+0.0	+148.8	0.0	15.6	0.8	
R Aql.............	+47.4	−0.3	8.2	1.4	4
IRC +10420	+73.7	...	33.0	...	5, 6
RR Aql	+27.8	+0.3	6.8	1.9	
NML Cyg	−1.2	−1.5	27.7	4.5	7, 8

NOTES.—(1) Morris *et al.* 1979: V_0(SiO) = +10.6±1.7, V_e(SiO) = 18.8±1.5. (2) Morris *et al.* 1979: V_0(SiO) = +17.6±1.5, V_e(SiO) = 36.7±2.0. (3) Wolff and Carlson 1982: V_0(SiO) = +22.3±2.3, V_e(SiO) = 32.3±2.4. (4) Morris *et al.* 1979: V_0(SiO)+48.7±0.8, V_e(SiO) = 7.7± 1.3. (5) Olofsson *et al.* 1982: V_0(SiO) = +77.5±1.5, V_e(SiO) = 33.7±2.0. (6) V_0(OH) is mean of total velocity range at 1612 MHz; high velocity peak is not well defined. (7) Morris *et al.* 1979: V_0(SiO) = +4.3±1.0, V_e(SiO) = 29.4±2.5. (8) Wolff and Carlson 1982: V_0(SiO) = −2.0±1.3, V_e(SiO) = 27.5±1.3.

determine V_0 is particularly advantageous since it is detectable for many stars.

The expansion velocity V_e is taken to be one-half the total velocity width of the OH emission, rather than the usually quoted value of one-half the peak separation (V_e^P). Differences between these values which are greater than the instrumental resolution of 0.6 km s^{-1} are not predicted in a spherical shell model with constant outflow velocity. Morris *et al.* (1979) indicate that V_e^P is systematically less than values of V_e derived from the full width of thermal SiO emission. However, we find good agreement between values of V_e derived from the *full width* of the OH profile and those derived from the SiO data.

The above result indicates that OH (1612) is subject to the same velocity field as the thermalized SiO which presumably arises throughout the extended envelope (Morris *et al.* 1979). It remains to be seen, however, as to whether the full width of either of these species gives the true expansion velocity. We discuss in § IVa the possibility of macroscopic streaming motions which can introduce an intrinsic uncertainty in determinations of V_0 and V_e.

c) Structure of the OH Maser Clouds

i) Morphology

For sources where the velocity range of the low or high velocity spectral feature is only a few km s^{-1} or less, the structure is relatively simple and changes very little. The structure is summarized for these stars in the Notes to Table 3. Maps and discussion of individual sources are presented in the Appendix for the more interesting cases where the spectral features extend over a large velocity range and are well resolved. In this section we summarize the overall properties of these latter sources.

At the peak velocities most of the sources exhibit simple structure dominated by a single knot or map maximum, in agreement with the prediction of "caps" of emission at these velocities (cf. Reid *et al.* 1977). A notable exception is OH 32.8−0.3 (see the Appendix).

At intermediate velocities maps of well-resolved spectral features are complex, consisting of knotlike (often unresolved) features and extended emission. Positions of the knots evolve smoothly with velocity, and the knots

can be followed typically over a velocity range ~ 4–5 km s^{-1}. From comparison to higher resolution data (Reid *et al.* 1977; Bowers *et al.* 1980; Norris, Diamond, and Booth 1982), it appears that the scale size of individual maser features can range from $\leq 0\overset{''}{.}05$ to $\geq 1''$ or $2\overset{''}{.}$

For some stars where emission is detected at $V \approx V_0$, there is evidence for an underlying spherical geometry based solely on the circular shape of the emission distribution (see the Appendix for OH 127.8−0.0, OH 26.5+ 0.6, and OH 32.8−0.3). At nearby velocities the emission distribution is asymmetric and clumpy, but it appears to outline portions of ringlike structures centered about the inferred stellar position. In some cases the maps also show evidence of front-back symmetry since similar asymmetric shapes are observed at velocities equidistant from the derived stellar velocity (e.g., OH 127.8−0.0 and VY CMa). Such symmetry provides an additional method to determine the stellar velocity.

In one case (VY CMa) the underlying shape appears to be elongated in excess of that expected from the noncircular beam. The elongated shape, the significant positional offset between the low and high velocity emission (Table 1), and the optical and infrared data suggest a disklike geometry for the envelope (see the Appendix).

ii) *Shell Radius*

The outer radius of the maser cloud is important because it provides a lower limit to the size of the circumstellar envelope and an estimate of the mass loss rate (BJS; Deguchi 1982; Huggins and Glassgold 1982). For an expanding envelope the angular radius R_0^A is given by:

$$R_0^A = R^A(V)\left[1 - \frac{(V - V_0)^2}{V_e^2}\right]^{-1/2}, \qquad (1)$$

where $R^A(V)$ is the angular radius at velocity V.

If the source is resolved and emission is present over a sufficiently wide velocity range, a reliable estimate of R_0^A can be determined by fitting equation (1) to the data. These fits are shown in the Appendix where individual sources are discussed (see SBJ for NML Cyg). To account for asymmetric distributions we have measured $R^A(V)$ as the maximum distance from the stellar location to the first contour level above the noise, with a correction for beam broadening. Typical measurement errors are $\pm 0\overset{''}{.}2$.

For these cases R^A increases as V approaches V_0 at velocities where the maps are not signal-to-noise limited, but the data are not well-fitted for a single value of R_0^A. The stronger emission complex generally tends to have a smaller radius, possibly due to our limited dynamic range. Separate curves for the low and high velocity data

are presented in the Appendix, and the average value of R_0^A is listed in Table 3.

For many sources the spectral features are narrow, so the above technique is not applicable. In these cases we list the maximum value of R^A and the corresponding velocity V in Table 3 and compute R_0^A from equation (1). This method obviously is less accurate for determining R_0^A since small errors in measuring R^A are translated to larger errors in R_0^A. Moreover, it is possible that all individual spectral components for a source could be unresolved but distributed over a large region, thus severely underestimating R_0^A. This is unlikely, however, based on comparison of the values of R^A in Table 3 to the angular diameters determined by BJS from integration over the low and high velocity ranges. Derived values or upper limits for R_0^A are probably accurate to within 50%.

Given R_0^A, the linear radius R_0 can be determined if the distance is known. Alternatively, it is possible to determine R_0 from high quality measurements of the radio light curve by measuring the phase difference between the low and high velocity peaks, since this should correspond to the light travel time across the shell if these peaks originate respectively from the near and far sides of the envelope (Jewell *et al.* 1979; Morris and Bowers 1980; Herman and Habing 1981; Bowers and Morris 1983).

In Table 3 we list estimated distances and values of R_0. Values of distance which are not in parentheses are taken from Table 1 of BJS, except for NML Cyg where we use the value for the Cyg OB2 Association (§ IV*b*). These distances are combined with values of R_0^A to find the values of R_0 not listed in parentheses.

The parenthetic values of distance are derived from the parenthetic values of R_0 which were obtained from phase lag measurements (Herman and Habing 1981). Those authors indicate that their values of R_0 may have uncertainties of a factor of 2, indicating a possible factor of 2 error in the distance estimates. Distances taken from BJS (and thus nonparenthetic values of R_0) also are likely to have possible errors of a factor of 2. We therefore list both determinations of distance and R_0 to give an indication of the errors. In some cases (e.g., U Ori), differences can be large.

Finally, we list estimates of the mass loss rate $\dot{M}$. The relation of the mass loss rate to the radius of the maser shell is discussed in § IV*c*.

iii) *Shell Thickness*

The radial shell thickness can be determined in two ways. For saturated masers in a spherical shell with constant outflow velocity, the ratio of the outer radius R_0 to the inner radius R of the maser cloud is:

$$R_0/R = 1 + (S_P/S_0)(V_{th}/V_e), \qquad (2)$$

TABLE 3
DISTANCES, SHELL RADII, AND MASS LOSS RATES

Star	Distance (kpc)	(R^A, V) (arcsec, km s^{-1})	R_0^A (arcsec)	R_0 (10^3 AU)	$\dot{M}$ (10^{-6} $M_\odot$ yr^{-1})	Comments; References
IRC +10011	0.5 (0.5)	2.2, +25.4	4.4	2.2 (2.2)	18, 26	1; a, b
OH 127.8−0.0 ...	3.3	...	1.9	6.3	80	2; c
OH 138.0+7.3 ...	2.4	≤ 0.5, −45.9	≤ 0.8	≤1.9	≤ 7.6	3 (?); c
OH 141.7+3.5 ...	3.7	≤ 0.5, −46.7	≤ 0.9	≤ 3.3	≤ 22	3 (?); c
IRC +50137	0.8	1.5, +18.3	3.0	2.4	11	2; a
U Ori............	0.2 (1.2)	< 0.5, −42.4	< 0.6	< 0.1 (0.6)	1.2	4; d
IRC +40156	1.4	0.6, −27.9	1.8	2.5	13	3; c
VY CMa	1.5	...	2.1	3.2	230	2; a
IRC −20197	0.7	≤ 0.6, +50.9	≤1.4	≤1.0	4.1	3 (?); a
WX Ser..........	1.0 (>1.4)	< 0.5, +13.4	<1.1	<1.1 (1.6)	> 2.5, 8	4; a, d
OH 17.7−2.0	5.4 (3.4)	0.7, +51.9	0.9	4.8 (3.1)	20	3; c
OH 26.5+0.6	2.2 (0.5)	...	3.5	7.7 (1.6)	3.9, 5.4	2; e, f
OH 25.1−0.4	9.1	< 0.7, +153.9	<1.4	<12.7	< 310	4; c
OH 32.8−0.3	4.3 (3.2)	...	2.2	9.5 (7.0)	30, 34	2; e, f
OH 39.7+1.5	1.4 (1.4)	1.2, +5.8	2.0	2.8 (2.8)	28	5; e
OH 39.9+0.0	7.7	0.7, +158.2	0.9	7.2	29	3; e
R Aql............	0.3	2.6, +53.7	4.0	1.2	0.8	1; d
IRC +10420	3.4	...	3.0	10.2	200	6; c
RR Aql..........	0.4 (0.9)	0.6, +31.4	1.0	0.4 (0.9)	1.8	1, 3; c
NML Cyg	1.8	...	3.0	5.4	160	1; a

COMMENTS.—(1) See maps of SBJ. (2) See Appendix. (3) Slightly resolved. (4) Unresolved. (5) Resolved; position angle ≈ 45°. (6) See maps of Bowers 1983.

REFERENCES FOR MASS LOSS RATES.—(a) Hyland *et al.* 1972 and this paper. (b) Knapp *et al.* 1982. (c) Eq. (3) of this paper. (d) Gehrz and Woolf 1971. (e) Engels 1982. (f) Werner *et al.* 1980.

where S_P and S_0 are, respectively, the flux densities at the peak velocity and the stellar velocity, $V_{\rm th}$ is the thermal velocity, and V_e is the expansion velocity (Olnon 1977). For the three spherical sources mentioned earlier, there is detectable emission at $V \approx V_0$, allowing us to determine the ratio S_P/S_0 from the Green Bank profiles. Adopting values of V_e from Table 2 and assuming $V_{\rm th} \approx 0.5$ km s^{-1}, we find $R_0/R = 3.9$, 4.2, and 2.6 for OH 127.8−0.0, OH 26.5+0.6, and OH 32.8−0.3, respectively. From the values of R_0 in Table 3, this result suggests that amplification lengths can be as large as a few thousand AU. For unsaturated masers the intensity contrast is larger for a given amplification length, so values of R_0/R determined by this method are upper limits.

In principle, it is also possible to determine the shell thickness by measuring the ring thickness for maps at $V \approx V_0$, but this method generally will provide only a lower limit to R_0/R. For a finite thermal velocity, the maximum amplification length occurs at the outer edge of the ring, so that the observed emission distribution is weighted toward the outer radius and the apparent thickness is less than the true thickness. In addition, the amplification length for tangential emission is small, so unsaturated emission is likely to dominate, again weighting the observed intensities toward the outer edge of the ring. The three sources discussed above have ringlike structure at $V \approx V_0$, but the effects described above

combined with a clumpy distribution, a small signal-to-noise ratio, and a finite beamwidth do not allow us to make a meaningful estimate of the shell thickness with this method.

IV. DISCUSSION

The sources fall into two categories: (1) those for which the spectral features are narrow and the data are consistent with an expanding spherical shell by virtue of positional coincidence of the peak or extreme velocity features; and (2) those for which maps can be made at velocities near the stellar velocity, so that the underlying geometry and the behavior of radius as a function of velocity can be examined. Only VY CMa shows convincing evidence for a disklike geometry, and in this case it is severely perturbed. For the remaining stars nearly coincident positions (≤ 0″.3) for the peak velocity features or ringlike geometries whose radii increase as $V \rightarrow V_0$ indicate expanding, spherical envelopes.

Nevertheless, a simple spherical model with a constant outflow velocity is not entirely adequate for the following reasons. (1) The clumpy emission distributions at most velocities indicate the presence of density/velocity perturbations. (2) Positional offsets up to ~ 0″.3 (~10% of the maser shell radius) are observed between the low and high velocity peaks for several stars. (3) In some cases (e.g., OH 32.8−0.3) the peak emission is

extended. (4) There is significant emission outside the peak velocities which is easily detected in profiles obtained with an adequate velocity resolution and signal-to-noise ratio.

Because maser emission depends on a coherent amplification length, it is sensitive to small changes in the velocity field or gas density. We discuss below how such changes affect the profiles and maps.

a) Velocity Field

The parabolic shapes of the $R^A(V)$ curves in the Appendix indicate that the dominant kinematic mode is radial expansion. For expansion at a constant velocity, the outer slopes of the peak spectral features should be virtually infinite. However, Table 2 shows significant spectral broadening ($V_e - V_e^P > 0.6$ km s^{-1}) for many stars. Table 2 also shows differences for ($V_0^W - V_0$) $\gtrsim 0.5$ km s^{-1} for several stars, indicating unequal amounts of broadening at the profile extremes. We discuss three possibilities which may contribute to the broadening for a spherical shell of gas.

i) Subsonic Turbulence

There may be considerable turbulent activity in the atmosphere of cool giants and supergiants due to the presence of convective cells, shock waves, etc., but the effects of subsonic turbulent motion at distances $\sim 10^2$–10^4 AU from the star cannot be large because of the low sound speed in these cooler regions. The model of Goldreich and Scoville (1976) predicts kinetic temperatures ranging from ~ 500 K at 100 AU to ~ 20 K at 10^4 AU, corresponding to sound speeds ranging from 1.8 km s^{-1} to 0.4 km s^{-1}. Turbulence could account entirely for the differences between V_e and V_e^P for some of the stars in Table 2 since the velocity resolution is ~ 0.6 km s^{-1}. However, there is no indication that turbulence is a dominant factor for most cases since stars with OH maser regions close to the star (e.g., U Ori) do not show systematically larger velocity differences than stars where the maser regions are much larger.

ii) Velocity Gradient

Maser profiles can be broadened if there is a radial velocity gradient, but there is no known mechanism which can produce a velocity increase > 0.5 km s^{-1} at radii $\gtrsim 1000$ AU where the 1612 MHz masers are located (Elitzur, Goldreich, and Scoville 1976; Deguchi 1982). Our data do not rule out the possibility of velocity gradients, but, like turbulence, these cannot be entirely responsible for the profile broadening. Unequal broadening of the low and high velocity edges and positional offsets of the peak features are not predicted by radial velocity gradients.

iii) Macroscopic Velocity Fluctuations (Streaming)

Random velocity fluctuations or organized motion (streaming) can produce emission at velocities more extreme than the peak velocities, and there are several reasons to suspect that such motion is present in some of these envelopes.

1. Significant differences between V_0^W and V_0 for some of the stars in Table 2 indicate different degrees of broadening on the near and far sides of the shells, as might be caused by streaming motions with a scale size less than a shell radius. The values of $V_e - V_e^P$ indicate that the amplitude of any such motion is $\lesssim 2$ km s^{-1} for most stars but can range to $\lesssim 7$ km s^{-1}.

2. Calculations by Deguchi (1982) of the intensity distribution of maser emission in circumstellar envelopes as a function of random velocity fluctuations ~ 1–2 km s^{-1} show that the blue and red peaks (or velocity extrema) can be separated in position by up to $\sim 10\%$ of the true shell size, as is the case for several of the stars in Table 1.

3. The Deguchi model also indicates that the structure at the peak velocities does not have to be a symmetric cap or ring. Elongated structure such as that for the redshifted peak feature ($V = 76$ km s^{-1}) of OH 32.8−0.3 can thus be explained.

In summary, the VLA and Green Bank data are consistent with an underlying smooth velocity curve onto which is superposed velocity fluctuations (other than subsonic turbulence) or streaming motions with amplitudes generally $\lesssim 2$ km s^{-1}. The velocity fluctuations may be produced by asymmetries in the mass ejection process, by interaction of the outflowing gas with the interstellar medium, or by energy input from external sources such as hot stars or supernovae. The latter possibility seems highly probable for VY CMa and NML Cyg, since profile broadening is largest for these two stars and they are located in close proximity to young stellar associations (§ IVb).

b) Density Distribution

The map structure is unlikely to be determined only by velocity fluctuations because of the persistence of identifiable arcsec clumps over a velocity range ≥ 4 to 5 km s^{-1}. Streaming or subsonic turbulence is important over smaller velocity ranges (§ IVa) and probably influences the spot ($\lesssim 0\rlap{.}''1$) distribution across an arcsec clump. However, it is likely that much of the map structure is determined by localized enhancements of the pump rate or the OH column density along the line of sight. A combination of density/velocity effects is consistent with the persistence of features over several km s^{-1} and with the impression from VLBI maps of an almost random collection of spots at neighboring velocities in a given clump.

Deguchi (1982) argues that density clumping cannot produce the double-peaked OH profile, but his argument assumes isotropic emission from each clump. This is unlikely since the probability that a photon is added to a given stream of radiation is largest in the radial directions (Morris and Bowers 1980). Furthermore, his model, based only on random velocity fluctuations, does not produce double-peaked profiles whose features have the classic shape of a steep outer edge and a gradually sloped inner edge.

The intensity of an individual arcsec clump tends to vary smoothly across the velocity range in which the clump is detected. If the clump represents an unresolved spot, this result suggests the emission is saturated. Alternatively, the clump might consist of a group of spots whose intensity is the sum of saturated and unsaturated emission. The intensity integrated over the shell at a given velocity is likely to be saturated based on time variability studies (Harvey et al. 1974).

Clumps in the maps may represent clumps $\sim 10^{15}$–10^{16} cm in the mass density distribution, clumps in the OH density distribution, or both. Mass density clumps can produce local variations in the 35 μm pump photons or in the number of OH molecules. Werner et al. (1980) have shown that cool dust capable of pumping the maser can be located at distances ≥ 1000 AU from the star, comparable to the outer radii of the maser shells (Table 3), so spatial variations in the pump rate cannot be eliminated. Similarly, if OH is produced by the collisional dissociation of H_2O or by formation on dust grains (particularly in the inner parts of the envelope), higher column densities would be expected in denser clumps of material (Kwok 1976; Goldreich and Scoville 1976).

Alternatively, the OH density distribution can deviate significantly from the mass density distribution because of photodissociation of H_2O and OH by interstellar ultraviolet radiation in the outer parts of the envelope (Goldreich and Scoville 1976; Scalo and Slavsky 1980; Deguchi 1982; Huggins and Glassgold 1982). An anisotropic UV flux can thus produce asymmetries in the observed maser distribution. The calculations of Huggins and Glassgold (1982) indicate that as the UV flux is increased, the radius of the maser shell should decrease because of a larger penetration depth for photons capable of dissociation. Since the envelopes may be relatively thick (§ IIIc[iii]), some map structure may be produced by UV radiation, and some may be produced by mass density effects.

To examine the possible effects of photodissociation on the morphology of the envelopes, we have used the catalog of Garmany, Conti, and Chiosi (1983) to search for O star candidates which may be responsible for asymmetries observed in the maps of the well-resolved sources. For each O star in the catalog within $\sim 2°$ of the OH/IR star, we compute an upper limit G to the UV continuum radiation field by assuming the OH/IR star is at the projected distance of the O star. Huggins and Glassgold (1982) indicate that the main contribution to photodissociation occurs at wavelengths of about 950 Å for OH and 1100–1850 Å for H_2O, but the photodissociation rates are very uncertain and depend on the shell structure. We compute the UV radiation field at 1025 Å and compare it to the "ambient" value G^0 for the solar neighborhood (Jura 1974).

The results are summarized in Table 4 which lists candidate O stars, the spectral type and distance (Garmany, Conti, and Chiosi 1983), the projected distance r_p, the position angle (P.A.) of the O star relative to the OH/IR star, and the ratio G/G^0. We list only O stars for which $G/G^0 \geq 1$.

The distances to VY CMa and NML Cyg are probably fairly reliable (Lada and Reid 1978; Morris and Jura 1983), so these stars are subject to intense, anisotropic UV radiation (Table 4). The complex structure of the maser shells and the large amount of apparent velocity

TABLE 4

O STAR CANDIDATES WHICH MAY INFLUENCE STRUCTURE
OF WELL-RESOLVED SOURCES

OH/IR Star	O Star	Sp.	Distance (kpc)	r_p (pc)	P.A. (degrees)	G/G^0
OH 127.8−0.0 ...	HD 8768	O9.5	1.6	30	323	≤ 0.9
	BD +60°261	O7.5	2.9	64	191	≤ 0.7
VY CMa	HD 57060	O7	1.5	42	317	8.2
	HD 47061	O9	1.5	34	306	6.9
OH 26.5+0.6	BD −4°4503	O7	2.9	38	315	≤1.1
	BD −6°4787	O8	1.0	24	235	≤ 0.9
	HD 172275	O6	1.8	62	168	≤ 0.7
OH 32.8−0.3	BD −0°3584	O8	2.1	15	133	≤16.2
NML Cyg[a]	Cyg 2, 3	O8	1.8	38	304	6.1
	BD +41°3804	O5	1.8	63	306	2.6
	Cyg 2, 7	O3	1.8	86	308	1.4

[a] Only the three strongest candidates of the Cyg OB2 association are listed.

streaming (Table 2) support this, but make comparison to existing model calculations difficult. The distances to the other OH/IR stars in Table 4 are more uncertain, but the envelope structure of OH 32.8−0.3 may be influenced by the associated O star if the model of Huggins and Glassgold is correct. OH emission in maps of the low velocity components appears to be absent in the projected direction of the O star, and the OH profile of this star shows evidence for significant velocity streaming.

We conclude that the underlying circumstellar envelopes are predominantly spherical for most of the stars, but that the observed OH maser distribution can deviate considerably from the idealized model, depending on the velocity field and OH density distribution. The best evidence for this is found for the sources OH 127.8−0.0, OH 26.5+0.6, and OH 32.8−0.3 which are well resolved with maps available at $V \approx V_0$. The structure of the emission regions shows clear evidence for spherical envelopes, even though emission at the peak velocities is not coincident (OH 26.5+0.6) or is not confined to "caps" of emission (OH 32.8−0.3). For several other resolved sources (IRC +10011, IRC +50137, NML Cyg), the emission could perhaps be explained by a complex, nonspherical distribution of the gas and dust, but such an explanation is not compelling if the effects of velocity streaming or UV photoproduction are considered. In addition, near coincidence of emission at the extreme velocities supports a spherical geometry. A number of other sources are unresolved or marginally resolved. The envelope structure of some of these might be due to a nonspherical distribution, but the approximate positional coincidence of the peak or extreme emission again suggests sphericity. Only VY CMa presents good evidence for a nonspherical distribution, but the OH distribution is very complex, likely due to the complicated region in which it is located.

c) Relation of Shell Radius to Mass Loss Rate

From preliminary examination of our data (BJS), we discovered that the radius of the 1612 MHz cloud is related to the mass loss rate and expansion velocity. Deguchi (1982) and Huggins and Glassgold (1982) subsequently indicated that this result is expected if the OH at large distances from the star is produced by UV photodissociation of H_2O. In Figure 1 we reexamine this relation using improved values of R_0 and $\dot{M}$.

To plot Figure 1, we have used parenthetic values of R_0 listed in Table 3, if available, since these are determined from phase lag measurements and thus are distance independent (§ IIIc). Each value of R_0 was multiplied by a small correction factor $[-0.2(V_e/15)^2 +0.9(V_e/15)+0.3]$ derived from Table 1 of Huggins and Glassgold (1982) to normalize it to an expansion velocity of 15 km s^{-1}.
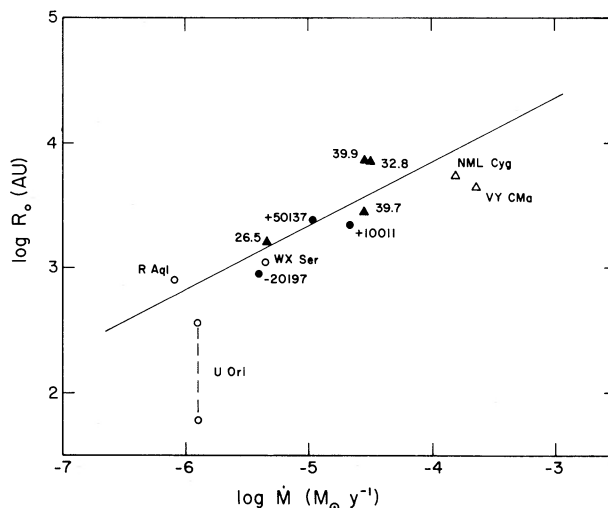

FIG. 1.—Angular radius of OH (1612 MHz) emission normalized to an expansion velocity of 15 km s^{-1} as a function of the estimated mass loss rate. Open and filled circles represent Mira variables with optical or IRC designations, respectively. Filled triangles represent radio luminous OH/IR stars discovered in galactic OH surveys. Open triangles represent M supergiants. The solid line is a plot of eq. (3).

The mass loss rates are derived from measurements of the depth of the 10 μm silicate absorption feature (Gehrz and Woolf 1971), from momentum conservation (Werner et al. 1980; Engels 1982), from model fitting to the infrared excess (Hyland et al. 1972), or from measurements of thermal CO emission (Knapp et al. 1982). Published values of $\dot{M}$ are scaled to the adopted (parenthetic) distances in Table 3, if appropriate. For stars observed by Hyland et al. (1972), we compute $\dot{M}$ by assuming that the gas to dust ratio is 100 and that the ratio of the outer to inner dust shell radius is large.

Values of R_0 are likely to be uncertain by about a factor of 2 (§ IIIc[ii]). Values of $\dot{M}$ are likely to have larger errors, although it is encouraging that the values derived by different techniques for IRC +10011 are comparable. Despite these errors, Figure 1 indicates the trend for R_0 to increase with $\dot{M}$. A least squares fit to the mean values of all the stars except VY CMa and U Ori gives:

$$\log R_0 (\text{AU}) = (5.89 \pm 0.16)$$

$$+ (0.51 \pm 0.27) \log \dot{M} \left(M_\odot \, \text{yr}^{-1} \right) \quad (3)$$

and is shown by the solid line in Figure 1. VY CMa was excluded because it appears to have a complex disklike geometry for which current photoproduction models are not appropriate. U Ori was excluded because of the large discrepancy in distance and thus R_0 (see the Appendix).

The fitted relation is in reasonably good agreement with the relation $R_0 \propto \dot{M}^{(0.69)}$ given in Figure 2 of Huggins and Glassgold (1982) for $V_e = 15$ km s^{-1}. The slightly smaller slope given in equation (3) may be due to the errors in the data. In addition, the theoretical relation implicitly assumes the expansion time scale is $\geq R_0^C/V_e$, where R_0^C is the characteristic radius for a given $\dot{M}$ and UV radiation field. Recent initiation of mass loss, star-to-star differences in the UV radiation field, or nonspherical geometries can cause deviations from the theoretical relation. In any case, although individual values may have considerable errors, the correlation in Figure 1 suggests that the relative values of $\dot{M}$ are approximately correct.

Equation (3) has been used to determine $\dot{M}$ for eight stars in Table 3 without previous estimates. Table 3 shows values of $\dot{M}$ ranging from 10^{-6} to $>10^{-4}$ $M_\odot$ yr^{-1}. The larger values are associated with the supergiant stars (VY CMa, IRC +10420, and NML Cyg), but these stars are extremely rare (Bowers and Kerr 1978; Bowers 1981; Engels 1982). Most of the stars in Table 3 are likely to be oxygen-rich Mira variables based on measurements of large amplitude, periodic infrared or radio light curves (Herman and Habing 1981; Engels 1982) and on the shapes of their OH profiles (Bowers and Kerr 1978). The range in their values of $\dot{M}$ is ~ 1 to 50×10^{-6} $M_\odot$ yr^{-1}. This range significantly influences their optical, infrared, and microwave properties, resulting in the trend seen in Figure 1 for $\dot{M}$ to be respectively larger for optical Miras, OH-IRC stars, and radio luminous OH/IR stars discovered in galactic OH surveys (cf. N-Q-Rieu *et al.* 1979; Bowers *et al.* 1980; Engels 1982).

It is clear that steady wind mass loss plays an important evolutionary role. The correlation in Figure 1 shows that, for the most part, the radius of the envelope exceeds the radius of the OH (1612) maser region, indicating a typical lower limit of ~ 1000 yr for the expansion time scale for these stars. This is confirmed for IRC +10011, for which the CO ($J = 2-1$) emission has a radius $\sim 1'$ (Knapp *et al.* 1982). Thus in this case, mass loss has occurred continuously for at least 7000 yr. For the mass loss rates in Table 3, it is concluded that these stars may typically lose $\gtrsim 0.1-0.2$ $M_\odot$ during this phase of their evolution, comparable to the estimated masses of planetary nebulae. The large mass loss rates make these stars significant contributors to the interstellar medium (Bowers and Kerr 1977).

d) Implications for Mass Loss Mechanisms

The result that most Mira variables have spherical circumstellar envelopes indicates that the origin of the wind is likely to be caused by mechanisms such as radiation-driven or shock-driven mass loss rather than mechanisms which predict large deviations from sphericity. Examples of the latter category include nonradial

pulsations (Schmidt, Angel, and Beaver 1978), rotationally forced ejection (Mufson and Liszt 1975; Kafatos and Michalitsianos 1979), and mass ejection in binaries (Morris 1981).

Nevertheless, there is a small number of evolved stars for which nonspherical circumstellar geometries have been found (see Zuckerman 1980; Cohen and Schmidt 1982). In some cases (VY CMa), the envelope may be due to remnant material from star formation (Herbig 1970) rather than bona fide mass loss in the post–main-sequence phase. However, most such stars are embedded in bipolar nebulae which are suggested progenitors of planetary nebulae (Calvet and Cohen 1978; Morris 1981). Since nonspherical circumstellar geometries are not common among evolved stars, we suggest that mass ejection in close binaries is the most attractive mechanism to explain the formation of bipolar nebulae (Morris 1981) and planetary nebulae with similar structures (Livio, Salzman, and Shaviv 1979). This suggestion is supported by the presence of binary nuclei in some planetary nebulae with bipolar shapes (Livio 1982).

e) Evolutionary Implications

The evolutionary status of the OH supergiants is not well understood, and they may be considerably different types of objects. Recent discussions are given by Lada and Reid (1978) for VY CMa; Mutel, Fix, and Benson (1979) for IRC +10420; and Morris and Jura (1983) for NML Cyg. We discuss below the remaining objects in Table 3, all of which are likely to be Mira variables (§ IVc).

The Mira variables in Table 3 are oxygen-rich (O > C) stars which span a probable mass range $\sim 1-9$ $M_\odot$ (Engels 1982; Jones *et al.* 1983; Kwok 1983). It is likely that many or all of these stars will form planetary nebulae, but the observational link between planetary nebulae and Mira variables with large mass loss rates ($\gtrsim 10^{-5}$ $M_\odot$ yr^{-1}) is not firmly established (Jones *et al.* 1983). However, the discussion of the previous section implies that the binary nature of the central object is an important consideration.

For example, an evolutionary sequence in which higher mass ($\gtrsim 2$ $M_\odot$) oxygen-rich stars pass through transition phases as carbon-rich (C > O) stars, bipolar nebulae, and subsequently planetary nebulae has been outlined by Zuckerman *et al.* (1976, 1978). We propose the following arguments to suggest this sequence occurs preferentially in binary systems.

1. Carbon-rich stars are much rarer than oxygen-rich stars (Blanco 1965), but a surprisingly large percentage of (perhaps all) carbon stars whose morphology has thus far been studied shows evidence for nonspherical circumstellar distributions, depending on the wavelength at which they are observed (see lists of Zuckerman 1980; Cohen and Schmidt 1982). In contrast, we have shown

that most oxygen-rich stars lose mass in spherical envelopes.

2. The mass loss rates for carbon stars ($\gtrsim 10^{-4}$ $M_\odot$ yr^{-1}) generally are larger than those for oxygen-rich Mira-type stars (Zuckerman *et al.* 1977, 1978; Knapp *et al.* 1982; Table 3 of the present paper). Knapp *et al.* (1982) concluded that a different (unspecified) mass loss mechanism is required for carbon-rich stars than for oxygen-rich stars. Models of mass ejection in binaries predict large mass loss rates (Livio, Salzman, and Shaviv 1979; Morris 1981).

3. Periods of variability > 1000 days have been found for some oxygen-rich Miras in Table 3 (Herman and Habing 1981; Engels 1982) and are much larger than those for known carbon stars. Thus not all oxygen-rich stars with extensive mass loss may become carbon stars, although it is possible that there are undiscovered, highly reddened carbon stars with comparable periods.

The above discussion leads to the following scenario for the formation of planetary nebulae. The system starts as a single star or wide binary in which an oxygen-rich Mira variable loses mass in a spherical outflow at a rate $< 10^{-4} M_\odot$ yr^{-1}. (A discussion of how the mass loss rate depends on the mass of the star and the time spent on the asymptotic giant branch is given by Jones *et al.* 1983). This phase produces the large, spherical halos found in some planetary nebulae (cf. Kwok 1981) and an oxygen-rich chemistry. The more massive single stars eventually may become carbon-rich by convective dredging (e.g., Iben 1981), but the circumstellar geometry should be spherical. Mira stars in Table 3 with large mass loss rates and evidence for spherical outflow are likely progenitors.

For a wide binary in which sufficient mass is lost from the system, the separation of the components decreases with time, the mass loss rate increases to a value $\geq 10^{-4}$ $M_\odot$ yr^{-1}, and the outflow becomes planar (Livio, Salzman, and Shaviv 1979; Morris 1981). A bipolar nebula (and subsequently a nonspherical planetary nebula) is formed. Since bipolar nebulae can be oxygen-rich or carbon-rich (Morris 1981), we suggest that the oxygen-rich star becomes carbon-rich as the outer envelope is lost in the bipolar phase.

Thus a binary system could produce objects with a mixed morphology, consisting of a low density, spherical region and a higher density, bipolar region. This might explain the morphologies found for objects such as the bipolar nebula OH 231.8+4.2 (Morris, Bowers, and Turner 1982), the carbon star IRC +10216 (McCarthy, Howell, and Low 1980; Knapp *et al.* 1982), and various planetary nebulae (Capriotti 1978). In this scenario, OH 231.8+4.2, which has an oxygen-rich envelope and whose central star is a Mira variable (Bowers and Morris 1983), may represent a transition object between an oxygen-rich, spherical mass loss phase and a carbon-rich, bipolar mass loss phase.

V. CONCLUSION

In this paper we have attempted to determine the structure of circumstellar envelopes associated with type II OH/IR stars by mapping the distribution of OH (1612) emission around these stars. The results indicate that most of the stars are surrounded by predominantly spherical, expanding envelopes, although for one star (VY CMa) there is evidence of a disklike geometry. The outer radii of the maser clouds range from ~ 100 AU to 10^4 AU and are correlated with the estimated mass loss rates which range from $\sim 10^{-6}$ $M_\odot$ yr^{-1} to 10^{-4} $M_\odot$ yr^{-1}.

The map structure at a given velocity can be complex, consisting of individual maser features ranging from $< 0\rlap{.}''05$ to $\geq 1''$ and distributed in ringlike structures. Maser features which persist over velocity intervals of a few km s^{-1} are due to clumps in the OH and possibly the mass density distribution with scale sizes $\sim 10^{15}-10^{16}$ cm. Other features in the maps may be the result of macroscopic velocity streaming superposed on the radial expansion curve. Evidence of front-back shell symmetry for some sources also indicates azimuthal density structure or velocity coherent pathlengths with a scale size comparable to the radius of the maser region. Subsonic turbulence and radial velocity gradients also may be present, but they cannot account for all the effects seen in the data.

Because of evidence for density clumping and velocity fluctuations, we estimate the accuracy to which the stellar position, radial velocity, and circumstellar expansion velocity can be determined from OH (1612) data. Our conclusions are as follows.

1.—*Stellar position*. If the signal-to-noise ratio is sufficiently large, we suggest that the mean position of the extreme velocity features is an indicator of the stellar position at the level of one-tenth of an arcsec. The mean position of the peaks is much easier to determine and is likely to be accurate to within a few tenths of an arcsec, but the positions of low and high velocity peaks can be separated by $\sim 10\%$ of the shell radius.

2. —*Stellar radial velocity*. This quantity can be determined from the mean velocity of the outer peaks, from a parabolic fit of the radius-velocity relation (eq. [1]), to the data, or from the presence of front-back symmetric structure in the maps. The results indicate that the mean velocity of the outer peaks gives V_0 to an accuracy of ± 1 km s^{-1}.

3.—*Circumstellar expansion velocity*. Estimates of V_e determined from the *full width* of the OH profile or from a fit of equation (1) to the VLA data agree with estimates derived from thermal SiO profiles, indicating that OH (1612) is subject to the same velocity field. An intrinsic uncertainty $\sim 1-2$ km s^{-1} may be present in derived values of V_e for both species because of the likely presence of streaming motions.

Finally, we discuss the implications of these results for mass loss mechanisms and subsequent evolution of evolved stars. The spherical envelopes associated with most OH Miras support models of radiation-driven or shock-driven mass loss and suggest that these stars may be responsible for the optical halos associated with some planetary nebulae. Because nonspherical circumstellar geometries are primarily associated with spatially rare objects, we suggest that they are produced from close binary systems. Examples of such objects are bipolar nebulae, nonspherical planetary nebulae, and carbon stars. A binary nature may explain the large mass loss rates for these objects ($\geq 10^{-4} M_\odot$ yr^{-1}) as well as the evidence for a mixed morphology (sphere + disk) detected for some of them.

APPENDIX

In this section we present Green Bank profiles, VLA maps, and discussion of sources for which the spectral features extend over a large velocity range and are well resolved. Each map gives the radial velocity and the peak map flux in the upper right corner. Contour levels and map origins are listed in the figure captions. For all sources, maps were made of alternate (independent) spectral channels, but to conserve space maps are presented for larger velocity intervals deemed to be adequate for showing the salient structural properties of each source.

a) OH 127.8−0.0

This source is the brightest OH/IR star in the anticenter region ($l > 90°$) and is coincident with the infrared source AFGL 230. High-resolution spectral-line maps obtained with the Jodrell Bank interferometer have been published by Norris, Diamond, and Booth (1982). These authors suggest the emission arises from an expanding spherical shell, but the peak velocity emission is offset by 0″2 of right ascension in their maps.

Selected VLA maps of this source are shown in Figure 2. We find the peak and extreme velocity features to be coincident at the position given in Table 1, unambiguously indicating the stellar position. At intermediate velocities, features emanate from the tangential portion of the shell and are centered about the stellar position. An underlying spherical geometry is indicated from the map at $V = -49.9$ km s^{-1} which appears to outline the entire shell.

The maps in Figure 2 indicate that the emission distribution is asymmetric relative to the star with the bulk of the emission arising from the eastern side of the shell. The asymmetry is present over a velocity range ~ 3 km s^{-1} near velocities of -63.5 and -47.6 km s^{-1}, equidistant from the stellar velocity of -55 km s^{-1}. This front-back symmetric structure can also be seen in the maps of Norris, Diamond, and Booth (1982).

The emission in Figure 2 is present at all position angles relative to the star, indicating that it arises throughout the 4π steradians of the shell. However, the front-back symmetry at $V \approx V_0 \pm 8$ km s^{-1} indicates an azimuthal structure with a scale size $\sim$ the radius of the envelope. This might be caused by (OH) density clumping or longer pathlengths of amplification along the line-of-sight in the eastern portion of the shell.

A plot of shell radius versus velocity is shown in Figure 3. The radii of red-shifted features ($V > V_0$) are systematically larger than the radii of blueshifted features at velocities symmetric to V_0. Curve 1 is a fit of equation (1) to the blueshifted features only; curve 2 represents an envelope to the data in an attempt to determine the maximum radius R_0^4 of the shell. For both curves the values of V_0 and V_e are taken from Table 2. We conclude that the shell structure is characterized by a predominantly spherical distribution whose outer radius of the maser shell varies from 1″6 to 2″2 with the largest dimension occurring on the eastern, far side of the shell.

b) IRC + 50137

The structure of this source (Fig. 4) is complex and changes rapidly with velocity. The map maxima and centroids of the emission distributions for the peak features at -14.0 and $+19.4$ km s^{-1} are offset by 0″3 entirely in the north-south direction. The centroid of the peak low velocity feature is more northerly but moves southward by $\sim 1''$ at intermediate velocities, while the peak high velocity emission is more southerly but moves northward at intermediate velocities.

The positional offset and the possibly complex structure of the peak spectral features are not consistent with a simple, spherical model in which they should appear as positionally coincident caps of emission. However, at some velocities (e.g., $V = -12.9$ km s^{-1}) the low-level contours suggest a circular shape consistent with an underlying spherical distribution. The rapid change of structure in small velocity intervals suggests that velocity fluctuations ~ 1 km s^{-1} may be responsible for much of the appearance of the maps. Further observations with better signal-to-noise and uv coverage are desirable.

c) U Ori

The time-dependent behavior of the OH emission from this star is extremely peculiar and has been re-
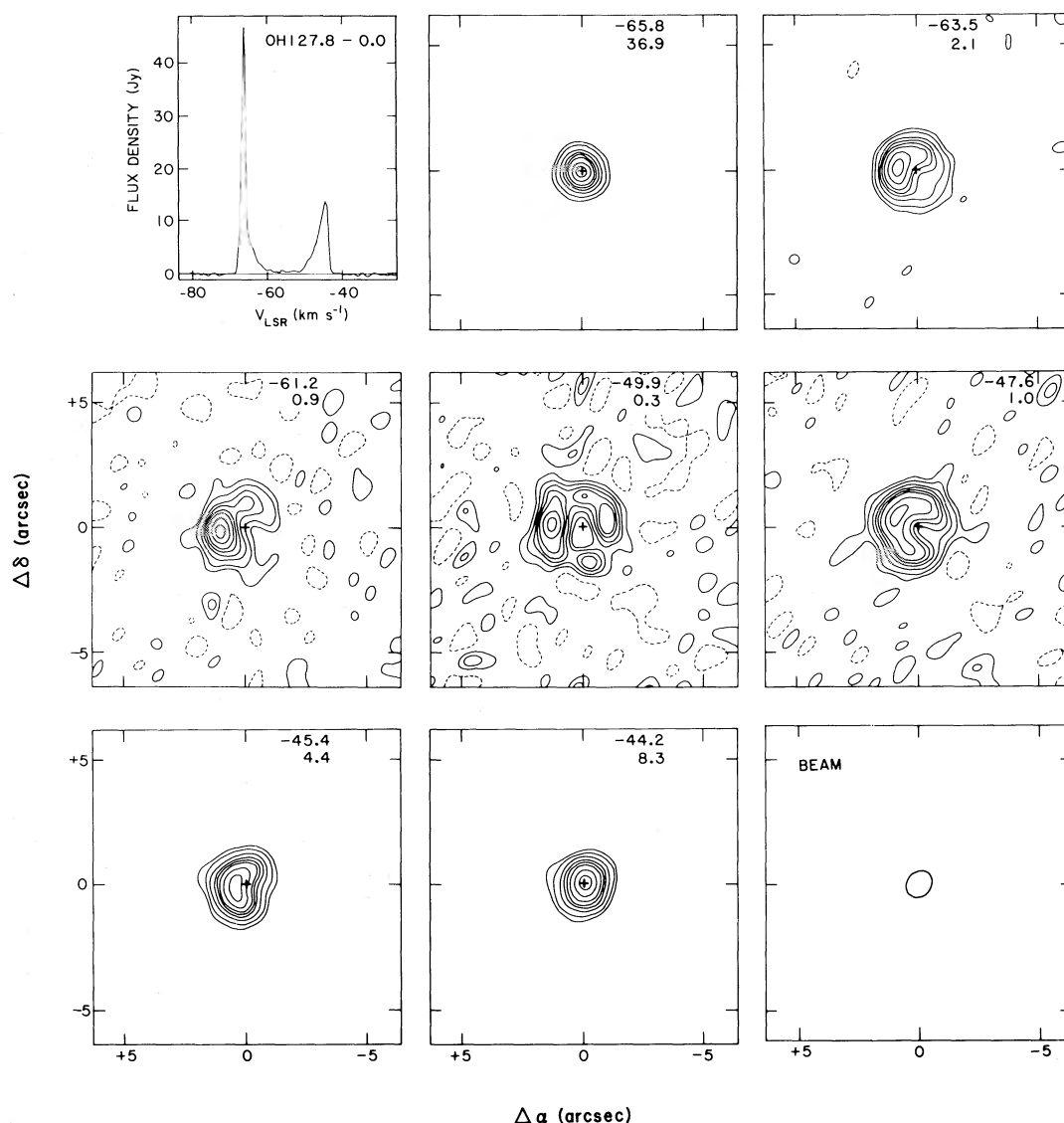
FIG. 2.—Intensity profile as a function of LSR radial velocity obtained at Green Bank, and VLA maps of the angular intensity distribution as a function of position and radial velocity for the source OH 127.8−0.0. LSR radial velocity and peak flux density per beam are given in the upper right corner of each map. The contour levels are in units of −5%, 5%, 10%, 20%, 30%, 40%, 50%, 70%, and 90% of the peak flux density. The cross designates the inferred stellar position (Table 1). The map origin is $\alpha(1950) = 01^h 30^m 27\overset{s}{.}63$, $\delta(1950) = +62°11'31\overset{''}{.}25$.

viewed by Jewell, Webber, and Snyder (1981). The star was first discovered to have strongest emission from the main-line transitions. The 1612 MHz emission flared in 1974 and subsequently has declined with the characteristics of a damped oscillator. The profile structure has changed with time for all the OH transitions, although a double-peaked 1612 MHz structure appears to have been present since 1978. Initial VLBI observations at 1612 MHz showed the presence of small ($\leq 0\overset{''}{.}03$) components distributed over a region $\sim 0\overset{''}{.}2$ in size (Reid et al. 1977). Further observations indicated that the ap-

parent sizes of the maser components were $> 0\overset{''}{.}03$ (Reid et al. 1979). VLBI data at 1665 MHz indicate compact components distributed over a region $\sim 0\overset{''}{.}4$ in size (Fix et al. 1980).

The Green Bank profile (not shown) has narrow components with fluxes of 2.3 Jy at $V = -47.0$ km s^{-1} and 3.7 Jy at -41.7 km s^{-1}. The values of V_0 and V_e in Table 2 are based on this profile, but we caution that the velocity field is complex so there is uncertainty as to the correct values of V_0 and V_e (cf. Jewell, Webber, and Snyder 1981). Both components are unresolved with the
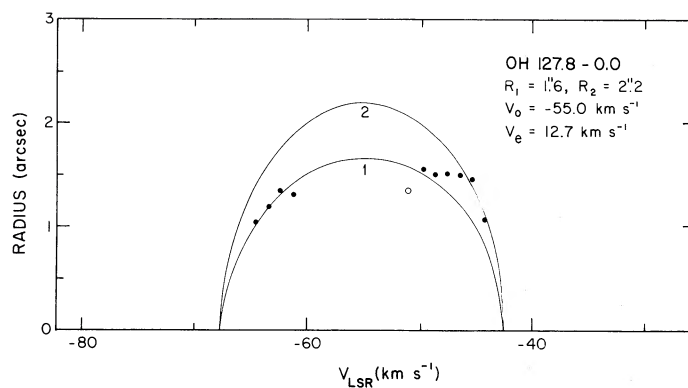
FIG. 3.—Angular radius of the OH (1612) emission distribution relative to the inferred stellar position as a function of LSR radial velocity for OH 127.8 − 0.0. Radii are measured to the first contour level above the noise and are corrected for beam broadening. Open circles denote values which are signal-to-noise limited. The two curves are plots of eq. (1), using the parameters given in the upper right corner.
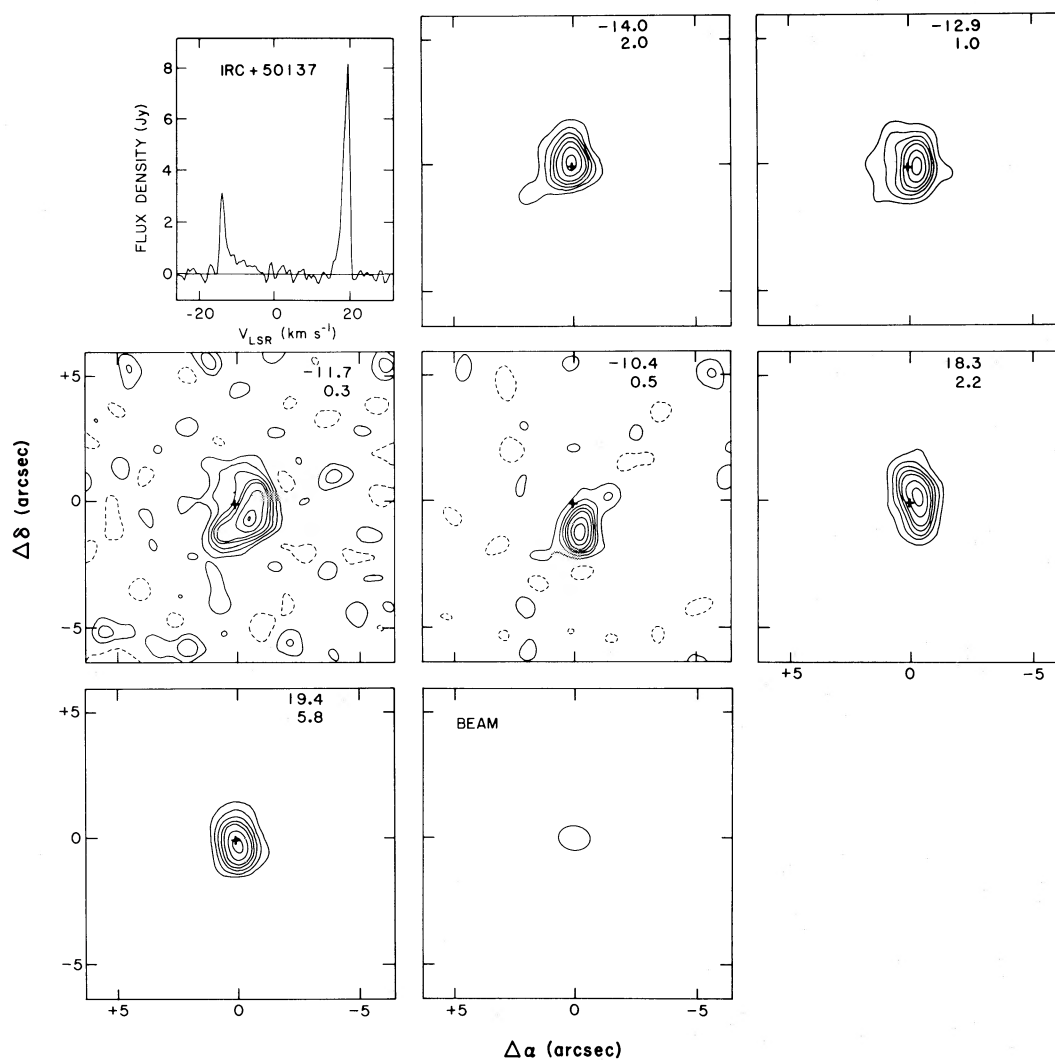

FIG. 4.—Profile and maps for IRC + 50137. Contour levels for each map are the same as in Fig. 2, except the lowest contour level which is ±10% of the peak flux density. The map origin is $\alpha(1950) = 05^h07^m19\overset{s}{.}67$, $\delta(1950) = +51°48'54\overset{''}{.}0$.

746
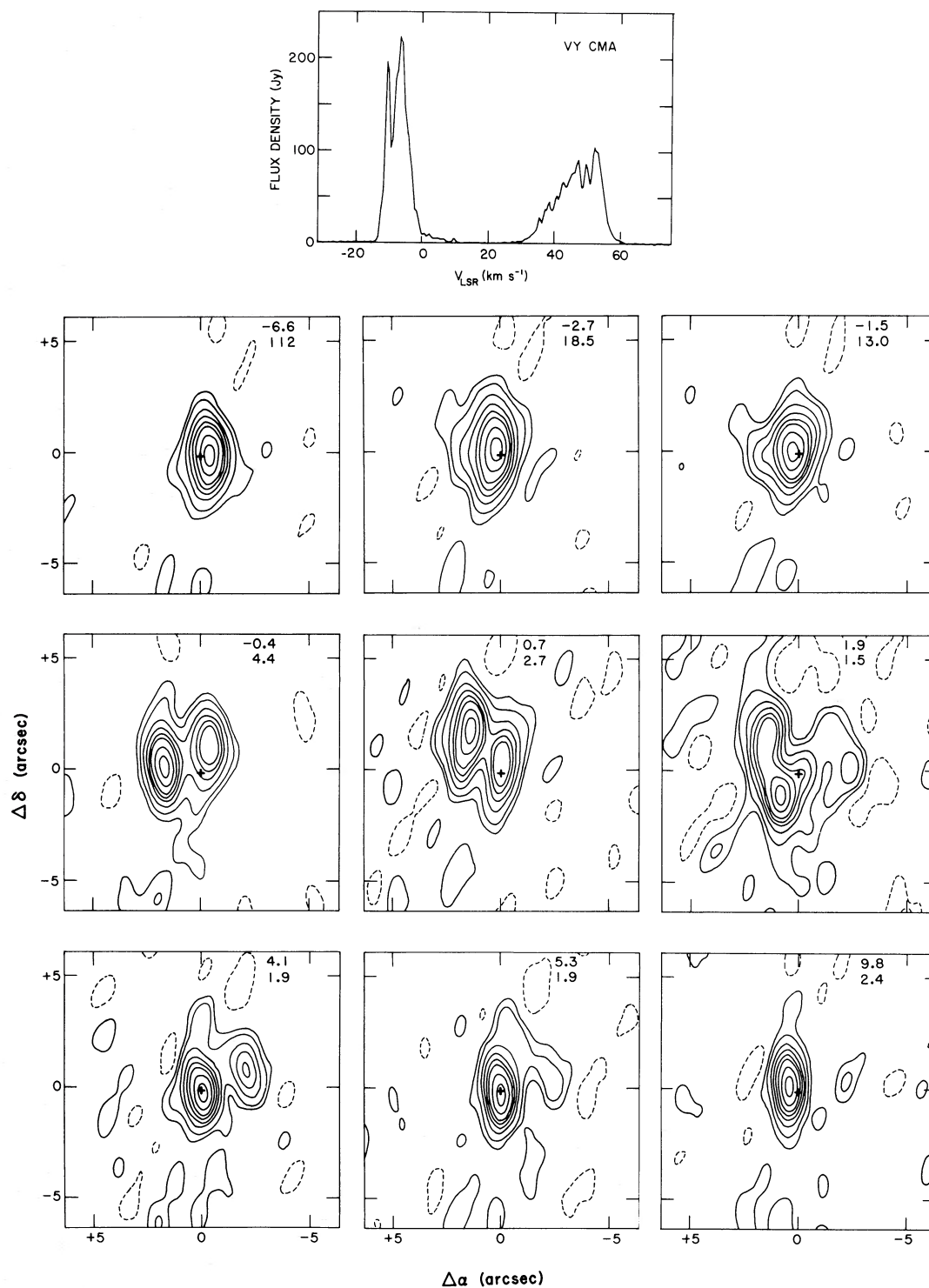
FIG. 5.—Profile and maps for VY CMa. Lowest contour level for each map is ±5% of the peak flux density and the map origin is α(1950) = 07^{h}20^{m}54^{s}74, δ(1950) = −25°40'12."25.

747
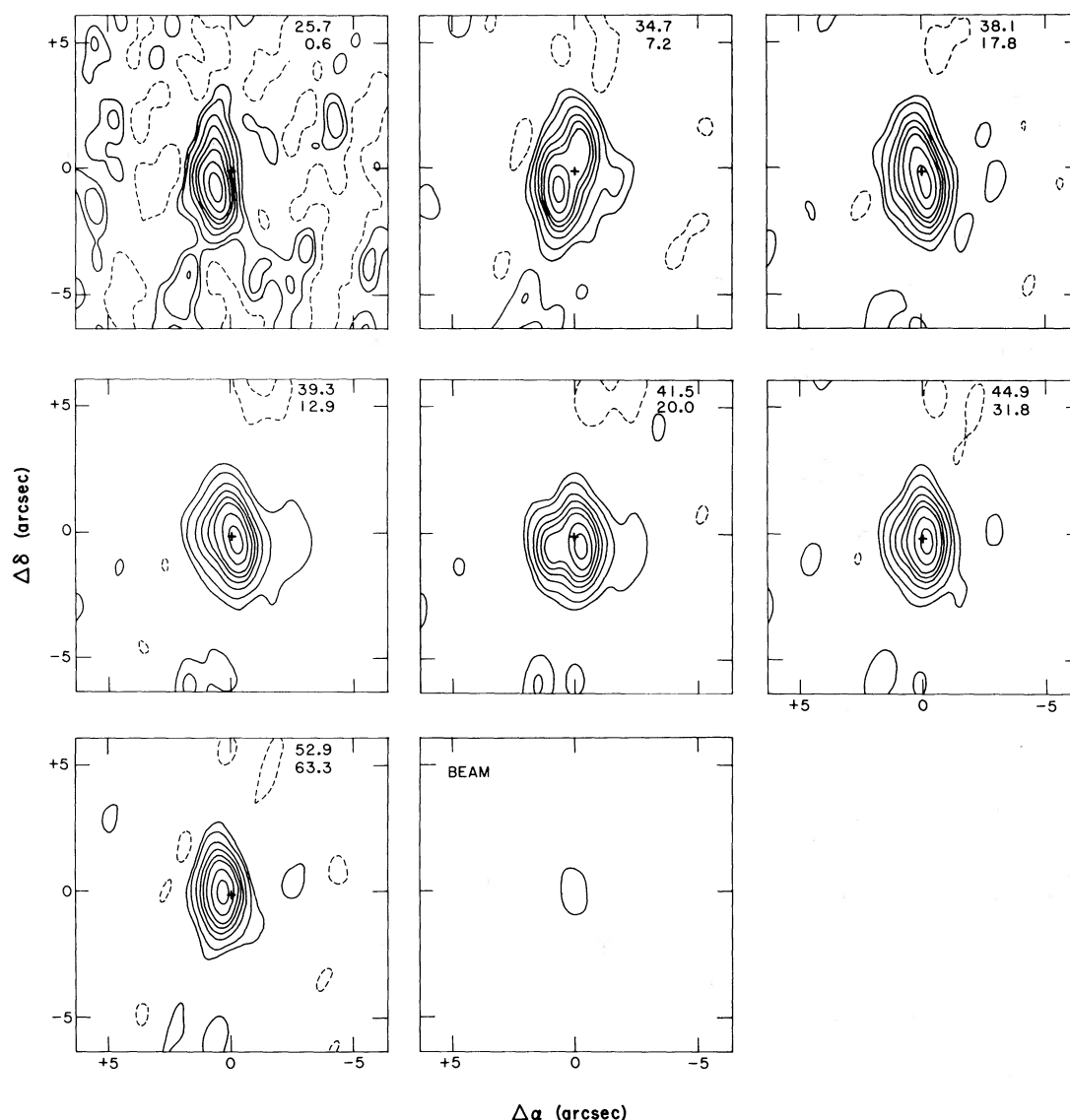
FIG. 5—Continued

VLA. At a distance of 200 pc derived from the period luminosity relation for Mira variables (Clayton and Feast 1969), the upper limit for the radius of the maser region is 100 AU which is anomalously small for the inferred mass loss rate according to the correlation in Figure 1 (also see BJS). If, however, the radius is ~ 600 AU as derived from phase lag measurements (Herman and Habing 1981), there is no anomaly but the inferred distance of 1.2 kpc in Table 3 is unreasonable unless this star is much more luminous than other Mira variables with comparable periods.

There is a positional offset of 0″.2 in right ascension between the components (Table 1). This might be caused by (1) a disklike geometry, (2) a significant rotational component, or (3) turbulent or streaming motions in the region of maser gain (§ IVa). The results elsewhere in this paper suggest that disklike geometries are rare for OH Mira variables, although OH 231.8+4.2 is an apparent exception (Morris, Bowers, and Turner 1982; Bowers and Morris 1983). U Ori is not a known binary or rapid rotator, so it is difficult to conceive how such a disk is present for this star but not for many other OH Mira variables. One remote possibility is that the magnetic field which is known to exist for this star (Reid et al. 1979) is stronger than average and is influencing the geometry of the mass outflow.

The possibility of a significant rotational component cannot be eliminated a priori because of the relatively

small radius of the maser region and the small expansion velocity. However, VLBI maps of individual velocity components suggest that another kinematic mode must be present; it is likely that the positions of the peaks are affected by turbulence in the maser region.

The peculiar properties of this star are by no means understood. It is possible that it is undergoing a short-lived but common phase in the evolution of maser

behavior associated with a recent onset of mass loss (BJS; Jewell, Webber, and Snyder 1981). Observations in the optical, infrared, and microwave regions should be continued.

d) VY CMa

This extremely peculiar M3–5 Ia star is embedded in nebulosity approximately $8'' \times 12''$ in extent and is projected onto the tip of a bright-rimmed cloud and molecular cloud complex at the edge of the H II region S310 in the young association NGC 2362 (Herbig 1970, 1972; Lada and Reid 1978). There are numerous lines of evidence that the circumstellar geometry is disklike based on optical and infrared observations (Herbig 1970, 1972; McCarthy 1979) and on the profile shapes of the SiO, H_2O, and OH (1667) microwave masers (cf. van Blerkom 1978; Morris and Bowers 1980). VLBI results suggest that the H_2O, OH (1665/1667), and OH (1612) transitions occur at respectively larger distances from the star, but they do not show clear evidence for disklike structure (Rosen et al. 1978; Reid and Muhleman 1978; Benson and Mutel 1979, 1982).

The complex but predominantly double-peaked 1612 MHz profile and representative VLA maps are shown in Figure 5. Maps of the stronger features are dynamic range limited. The structure changes very little over a velocity interval of about 8 km s^{-1} at each outer edge of the profile. The beam is highly noncircular, but there is some indication of elongation in the north-south direction. More importantly, there is a systematic displacement between the positions of the map maxima for the low velocity ($V = -12.9$ to -4.9 km s^{-1}) and high velocity ($V = 47.2$–55.2 km s^{-1}) emission. The velocity coverage for the VLA data is less than the total velocity
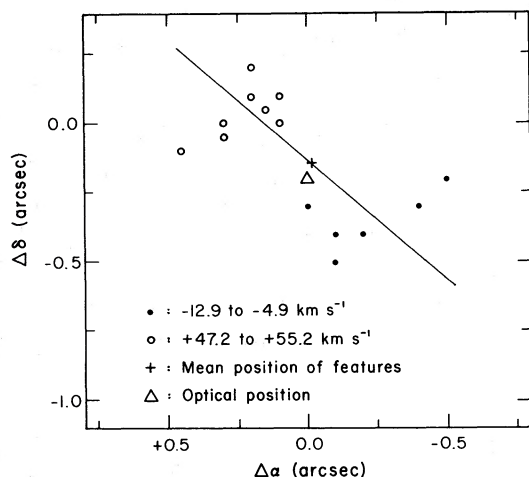

FIG. 6.—Positions of map maxima for the indicated low (*filled circles*) and high (*open circles*) velocity ranges of VY CMa relative to the map origin given in Fig. 5. The straight line is drawn through the average position of each cluster and represents the projected polar axis of the gas distribution (position angle = 50°). The derived position in Table 1 (corresponding to the mean position of the clusters) and the optical position of VY CMa given by Reid et al. 1981 are indicated by the cross and triangle, respectively.
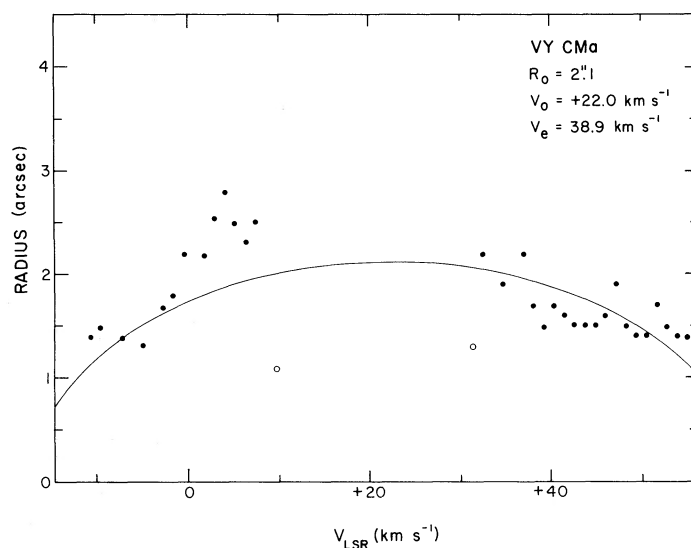

FIG. 7.—Same as Fig. 3 for the source VY CMa
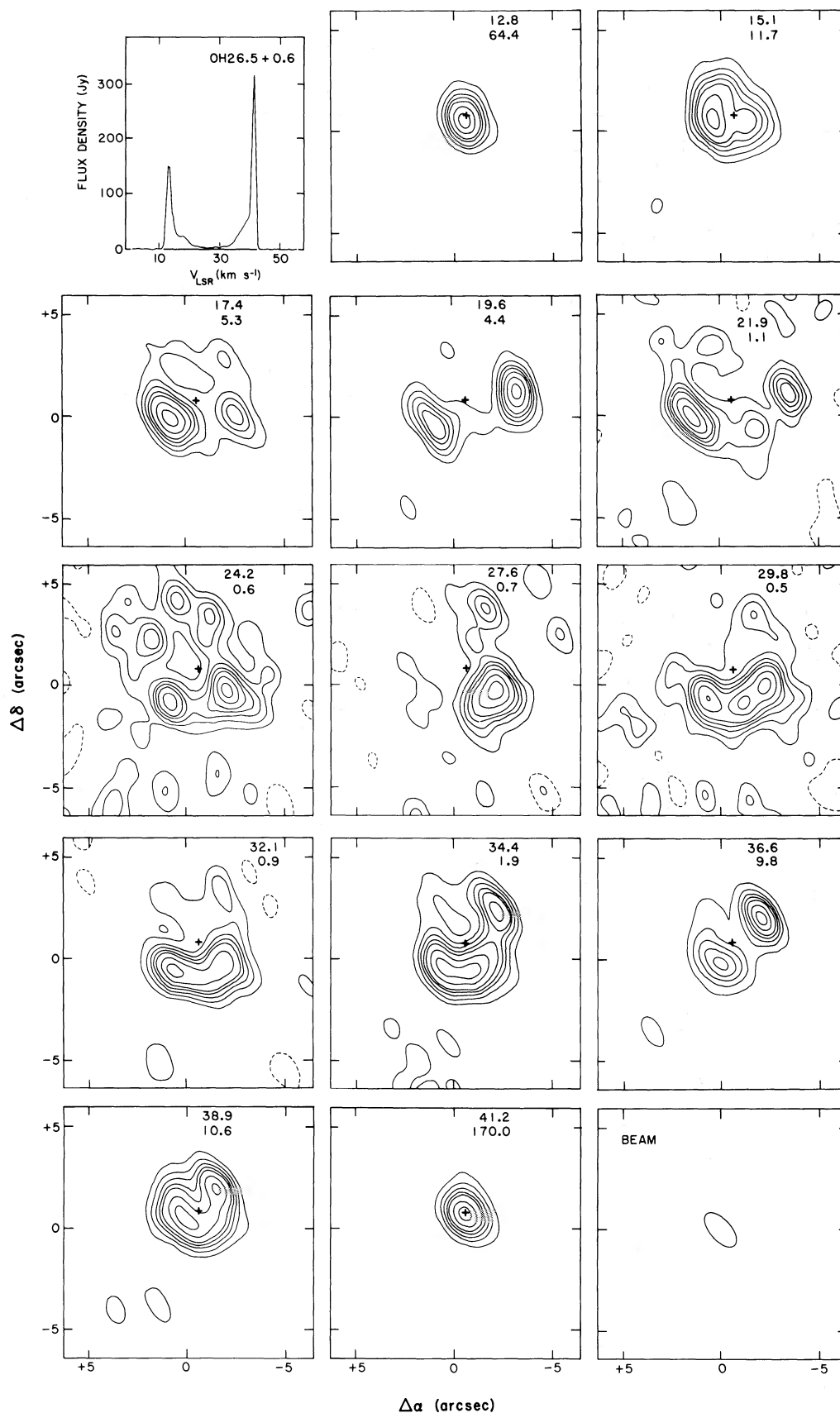
FIG. 8.—Profile and maps for OH 26.5 + 0.6. Lowest contour level for each map is ±10% of the peak flux density, and the map origin is α(1950) = 18^{h}34^{m}52^{s}50, δ(1950) = −05°26′38″0.

width of emission from VY CMa, so maps of extreme velocity features are not available.

The position of the map maxima for the above velocity ranges are plotted in Figure 6. The low and high velocity range are spatially separated and clustered in regions with scale sizes of a few tenths of an arcsec. Channel-to-channel position differences in each cluster are likely due to small velocity fluctuations (§ IVa). The spatial segregation of the low and high velocity components is significant because it persists over many km s^{-1} and thus reflects the (OH) density distribution.

The solid line in the figure is drawn through the average position of each cluster and has a position angle of 49° from the north. The mean position of both clusters is listed in Table 1 as our derived stellar position, and it is in excellent agreement with the optical position given by Reid, Moran, and Johnston (1981). We argue that this strongly indicates that the 1612 MHz emission is distributed in a tilted, expanding disklike or ringlike geometry with the solid line in Figure 6 indicating the projected polar axis. The line of nodes formed by the intersection of the plane of the disk with the plane of the sky is then oriented approximately northwest-southeast at a position angle of 140° (320°). This is similar to the position angle found by McCarthy (1979) for a flattened disk (1.1×10^{16} cm×1.7×10^{16} cm) at 10.2 μm.

A plot of angular radius versus velocity is shown in Figure 7. Points between +10 and +30 km s^{-1} are not shown because the data are signal-to-noise limited. If we also exclude the points between $0 \lesssim V \lesssim +5$ km s^{-1}, the data are reasonably well fitted by a parabola with $R_0 = 2\farcs1$, $V_0 = 22$ km s^{-1}, and $V_e = 39$ km s^{-1}. The values of V_0 and V_e agree well with those derived from the Green Bank profiles (Table 2).

Though Figure 7 shows an increasing radius as $V \rightarrow V_0$, the increase is not confined to the line of nodes, as would be the case for a flat, thin disk. At most intermediate velocities (-5 to $+47$ km s^{-1}), emission is primarily eastward of the star, but there is an extension to the northwest at velocities between $+2$ and $+5$ km s^{-1} which contributes to the anomalous values of radius in Figure 7. An apparent eastern bulge superposed on the north-south geometry is present at velocities of -5 to -1 km s^{-1} and $+39$ to $+45$ km s^{-1}, symmetric to the stellar velocity $V_0 \approx 21$ km s^{-1}. The bulge is present at the same location at both low and high velocities, indicating that a thin expanding disk model is not valid.

We propose an underlying thick disk or ellipsoidal geometry in which the 1612 MHz emission at the extreme velocities is confined to the plane of the disk. The small ratio of the displacement of these emission features ($\sim 0\farcs5$) to the disk radius ($\sim 2''$) suggests that the plane of the disk is highly inclined to the plane of the sky. This result is supported by the double-peaked structure of the OH (1612) and OH (1667) profiles (Morris and Bowers 1980) and by the triple-peaked structure of the H$_2$O and SiO maser profiles (van Blerkom 1978).

Assuming the disk is highly inclined to the plane of the sky, then emission at intermediate velocities emission occurs at high latitudes eastward of the line of nodes. High latitude emission westward of the lines of nodes may not be present because of the influence of the O stars in Table 4 which provide a considerable UV radiation field in this direction. It is noteworthy, however, that the map structure changes significantly over small velocity intervals at intermediate velocities, suggesting significant velocity fluctuations at high latitudes in agreement with the results of Table 2.
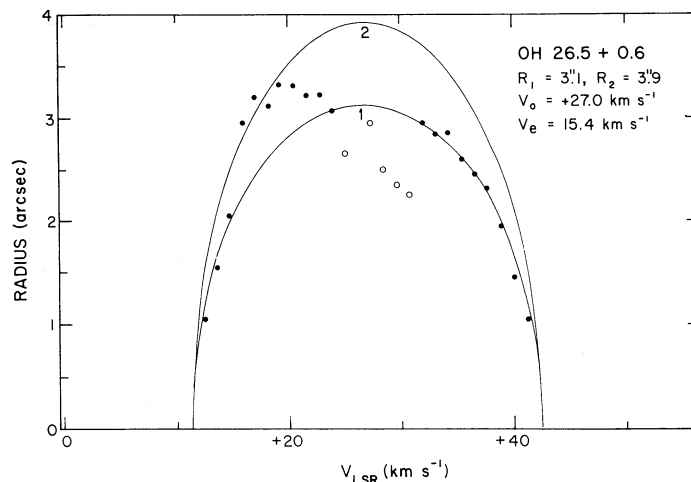

OH 26.5 + 0.6
R_1 = 3$\farcs$1, R_2 = 3$\farcs$9
V_0 = +27.0 km s^{-1}
V_e = 15.4 km s^{-1}

RADIUS (arcsec)

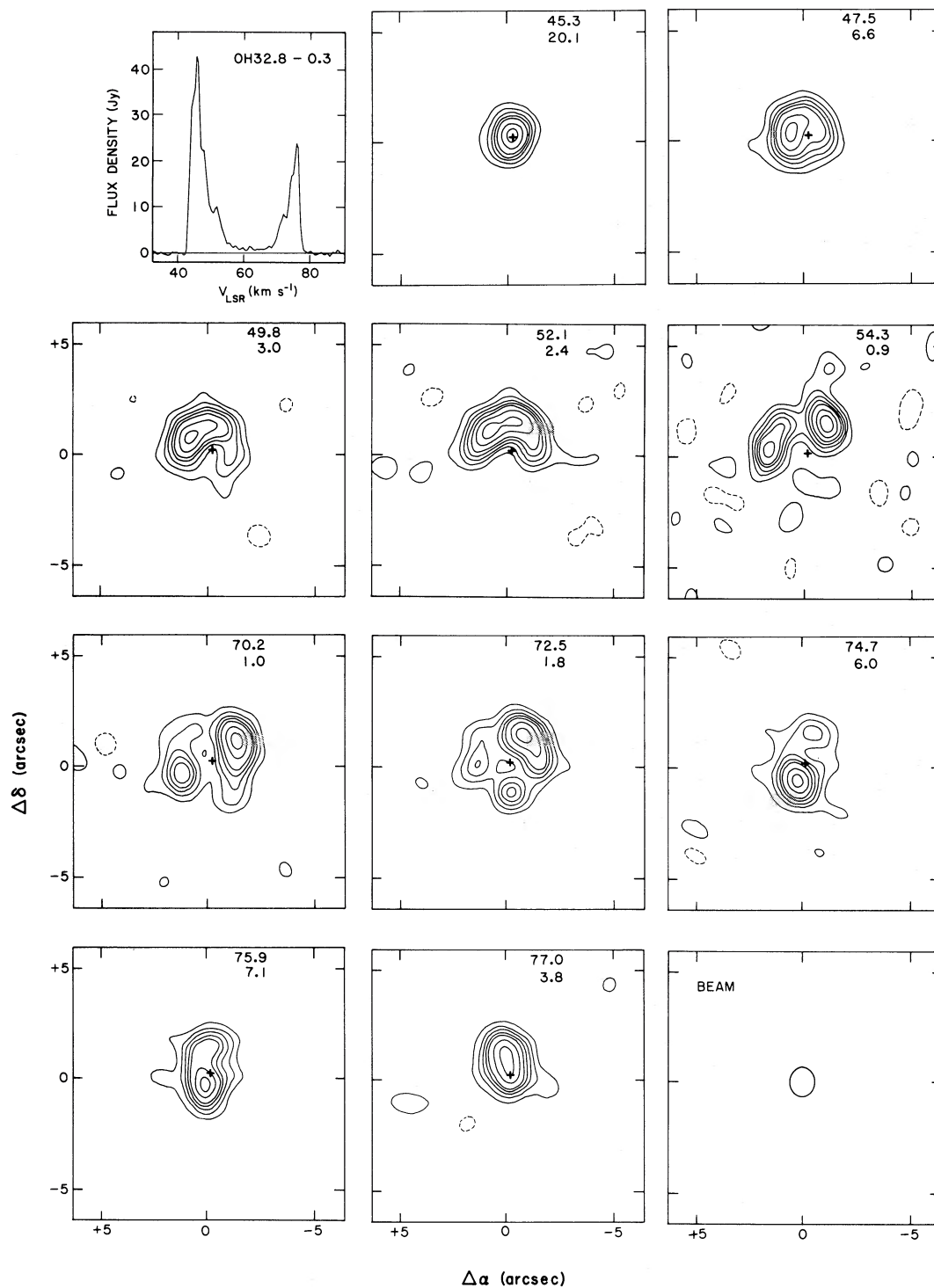V_{LSR} (km s^{-1})

FIG. 9.—Same as Fig. 3 for the source OH 26.5 + 0.6

FIG. 10.—Profile and maps for OH 32.8 − 0.3. Lowest contour level for each map is ±10% of the peak flux density, and the map origin is α(1950) = 18^{h}49^{m}48^{s}17, δ(1950) = −0°17′53″75.

e) OH 26.5+0.6

Previous VLA maps of this bright, well-resolved OH/IR star have been published by Baud (1981) who concluded that the data are consistent with an expanding shell model. Our data (obtained with a better velocity resolution and signal-to-noise ratio) support this, but our interpretation of the shell structure is different.

As noted in § IIIa, the derived stellar position in Table 1 is based on the position of the extreme velocity features at $V \approx +11.7$ and $+42.3$ km s^{-1}; the peak features ($V \approx +12.8$ and $+41.2$ km s^{-1}) differ from this position by $0\rlap{.}''3$ in declination and are offset from each other by $0\rlap{.}''2$. Baud did not note the discrepancy between the peak positions, probably because of his poorer velocity resolution (2.3 km s^{-1}). His published position agrees well with ours because it is derived from emission centered at $+10.4$ and $+42.2$ km s^{-1}.

Relative to the derived stellar position, Figure 8 clearly shows that the radius of the OH cloud generally increases at velocities closest to the stellar velocity, if the effects of clumpiness and signal-to-noise ratio are considered. At most velocities the emission tends to form a partial shell which wraps around the stellar position with most of the emission distributed between position angles of 90° and 320° relative to the star; at $V = +24.2$ km s^{-1} the outline of the complete shell is present. Detailed comparison of Figure 8 to Baud's maps suggests that the emission may be clumpier than suggested by him since there are various velocities at which the maps tend to be a collection of unresolved knots which outline various parts of the shell (e.g., $V = 17.4$, 19.6, 21.9, 24.2, and 36.6 km s^{-1}). At other velocities, however, the emission appears to be more uniformly distributed (e.g., $V = +29.8$, 32.1, 34.4, and 38.9 km s^{-1}). This result agrees with higher resolution measurements of circumstellar shells which show evidence for both small scale structure (often unresolved even with VLBI baselines) and much larger scale structure.

A plot of radius versus velocity is shown in Figure 9. Empty circles indicate maps which are signal-to-noise

limited. As with OH 127.8−0.0 whose structural properties are similar, two curves are fitted to the data. Curve 1 is a fit to the redshifted radii, and curve 2 is an envelope to the blueshifted radii. The maps show that the larger radii between $+16$ and $+23$ km s^{-1} are due to a tight knot of emission west of the star. There is also an intensity peak in this velocity range in the Green Bank profile.

The positional coincidence of the high and low velocity extremes, the presence of emission at all position angles relative to the star, and the circularly symmetric distribution of emission at $V = 24.2$ km s^{-1} indicate a spherical distribution in which the maser emission is distributed throughout the 4π steradians of the shell. The asymmetric intensity distributions suggest that the azimuthal (OH) density distribution at a given radius can vary considerably. The outer radius of the shell appears to vary from $3\rlap{.}''1$ to $3\rlap{.}''9$ with the maximum radius on the western, near side of the shell (due to the unresolved knot of emission). There is no compelling evidence for the inner ringlike structure or the increased mass loss rate with time suggested by Baud (1981).

f) OH 32.8−0.3

The Green Bank profile in Figure 10 shows a remarkable symmetry of the velocities of the secondary peaks relative to the stellar velocity. Peaks occur at approximately $V_0 \pm 15$, $V_0 \pm 14$, and $V_0 \pm 10$ km s^{-1}, as might be expected from concentric shells of gas expanding at different velocities. The VLA maps in Figure 10 do not show clear evidence for multiple shells, but the velocity resolution and signal-to-noise ratio are poorer than for the Green Bank profile.

The maps suggest a spherical distribution with tangential emission at $V = +72.5$ km s^{-1} outlining most of the shell. At other velocities knotlike features are distributed around the circumference of the shell, but only portions of the shell are seen at a given velocity. The radii of the redshifted distributions are consistently larger than those of the blueshifted distributions, and
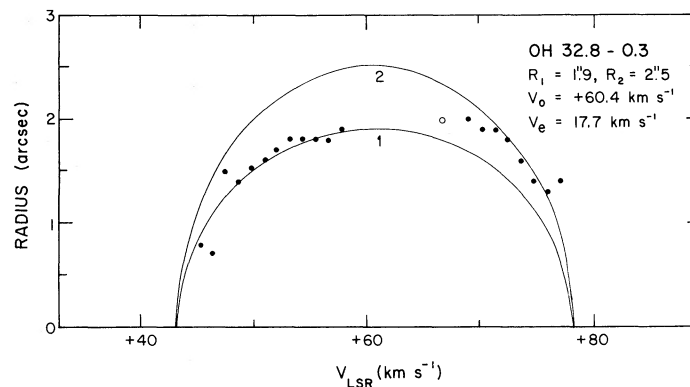

FIG. 11.—Same as Fig. 3 for the source OH 32.8−0.3

two parabolic curves are fitted to the radius-velocity data in Figure 11. The morphology of the maps suggests an inhomogeneous spherical shell whose outer radius varies from $1\overset{''}{.}9$ on the near side to $2\overset{''}{.}5$ on the far side.

Neither the positions of the map maxima for the outer peaks nor for the extreme velocity features are coincident. The high velocity peak emission is notably extended and elongated, probably due to significant velocity fluctuations in the shell (Table 2 and § IVa). Our derived stellar position is based on the positions of the low velocity extreme ($V \approx 43.0$ km s^{-1}) and peak ($V \approx 45.3$ km s^{-1}) emission as well as the geometric center of the high velocity peak emission ($V \approx 75.9$ km s^{-1}). These three positions agree to within $\pm 0\overset{''}{.}1$ and appear to represent the geometric center of the overall cloud.

REFERENCES

Baars, J. W. M., Genzel, R., Pauliny-Toth, I. I. K., and Witzel, A. 1977, *Astr. Ap.*, **61**, 99.
Baud, B. 1981, *Ap. J. (Letters)*, **250**, L79.
Benson, J. M., and Mutel, R. L. 1979, *Ap. J.*, **233**, 119.
———. 1982, *Ap. J.*, **253**, 199.
Blanco, V. M. 1965, in *Stars and Stellar Systems*, Vol. 5, *Galactic Structure*, ed. A. Blaauw and M. Schmidt (Chicago: University of Chicago Press), p. 241.
Bowers, P. F. 1981, *A.J.*, **86**, 1930.
———. 1983, *Ap. J.*, submitted.
Bowers, P. F., Johnston, K. J., and Spencer, J. H. 1981, *Nature*, **291**, 382 (BJS).
Bowers, P. F., and Kerr, F. J. 1977, *Astr. Ap.*, **57**, 115.
———. 1978, *A.J.*, **83**, 487.
Bowers, P. F., and Morris, M. 1983, *Ap. J.*, in press.
Bowers, P. F., Reid, M. J., Johnston, K. J., Spencer, J. H., and Moran, J. M. 1980, *Ap. J.*, **242**, 1088.
Calvet, N., and Cohen, M. 1978, *M.N.R.A.S.*, **182**, 687.
Capriotti, E. G. 1978, in *IAU Symposium 76, Planetary Nebulae*, ed. Y. Terzian (Dordrecht: Reidel), p. 263.
Clayton, M. L., and Feast, M. W. 1969, *M.N.R.A.S.*, **146**, 411.
Cohen, M., and Schmidt, G. D. 1982, *Ap. J.*, **259**, 693.
Deguchi, S. 1982, *Ap. J.*, **259**, 634.
Elitzur, M., Goldreich, P., and Scoville, N. 1976, *Ap. J.*, **205**, 384.
Engels, D. 1982, Ph.D. thesis, Bonn University.
Fix, J. D., Mutel, R. L., Benson, J. M., and Claussen, M. L. 1980, *Ap. J. (Letters)*, **241**, L95.
Garmany, C. D., Conti, P. S., and Chiosi, C. 1983, *Ap. J.*, submitted.
Gehrz, R. D., and Woolf, N. J. 1971, *Ap. J.*, **165**, 285.
Genzel, R., Pauliny-Toth, I. I. K., and Witzel, A. 1976, Tech. Ber. 30 (Max-Planck-Institut für Radioastronomie, Bonn).
Goldreich, P., and Scoville, N. 1976, *Ap. J.*, **205**, 144.
Harvey, P. M., Bechis, K. P., Wilson, W. J., and Ball, J. A. 1974, *Ap. J. Suppl.*, **27**, 331.
Herbig, G. H. 1970, *Ap. J.*, **162**, 557.
———. 1972, *Ap. J.*, **172**, 375.
Herman, J., and Habing, H. J. 1981, in *Physical Processes in Red Giants*, ed. I. Iben, Jr. and A. Renzini (Dordrecht: Reidel), p. 383.
Högbom, J. A. 1974, *Astr. Ap. Suppl.*, **15**, 417.
Huggins, P. J., and Glassgold, A. E. 1982, *A.J.*, **87**, 1828.
Hyland, A. R., Becklin, E. E., Frogel, J. A., and Neugebauer, G. 1972, *Astr. Ap.*, **16**, 204.
Iben, I. 1981, in *Physical Processes in Red Giants*, ed. I. Iben, Jr. and A. Renzini (Dordrecht: Reidel), p. 3.
Jewell, P. R., Elitzur, M., Webber, J. C., and Snyder, L. E. 1979, *Ap. J. Suppl.*, **41**, 191.
Jewell, P. R., Webber, J. C., and Snyder, L. E. 1981, *Ap. J.*, **249**, 118.
Jones, T. J., Hyland, A. R., Wood, P. R., and Gatley, I. 1983, *Ap. J.*, **273**, 669.
Jura, M. 1974, *Ap. J.*, **191**, 375.
Kafatos, M., and Michalitsianos, A. G. 1979, *Ap. J. (Letters)*, **228**, L115.
Knapp, G. R., Phillips, T.G., Leighton, R. B., Lo, K. Y., Wannier, P. G., and Wootten, H. A. 1982, *Ap. J.*, **252**, 616.

Kwok, S. 1976, *J.R.A.S. Canada*, **70**, 49.
———. 1981, in *Physical Processes in Red Giants*, ed. I. Iben, Jr. and A. Renzini (Dordrecht: Reidel), p. 421.
———. 1983, in *IAU Symposium 103, Planetary Nebulae*, ed. W. D. Flower (Dordrecht: Reidel), p. 293.
Lada, C. J., and Reid, M. J. 1978, *Ap. J.*, **219**, 95.
Livio, M. 1982, *Astr. Ap.*, **105**, 37.
Livio, M., Salzman, J., and Shaviv, G. 1979, *M.N.R.A.S.*, **188**, 1.
McCarthy, D. W. 1979, in *IAU Colloquium 50, High Angular Resolution Stellar Interferometry*, ed. J. Davis and W. J. Tango (University of Sydney), p. 18–1.
McCarthy, D. W., Howell, R., and Low, F. J. 1980, *Ap. J. (Letters)*, **235**, L27.
Morris, M. 1981, *Ap. J.*, **249**, 572.
Morris, M., and Bowers, P. F. 1980, *A.J.*, **85**, 724.
Morris, M., Bowers, P. F., and Turner, B. E., 1982, *Ap. J.*, **259**, 625.
Morris, M., and Jura, M. 1983, *Ap. J.*, **267**, 179.
Morris, M., Redman, R., Reid, M. J., and Dickinson, D. F. 1979, *Ap. J.*, **229**, 257.
Mufson, S. L., and Liszt, H. S. 1975, *Ap. J.*, **202**, 183.
Mutel, R. L., Fix, J. D., and Benson, J. M. 1979, *Ap. J.*, **228**, 771.
Nguyen-Q-Rieu, Laury-Micoulaut, C., Winnberg, A., and Schultz, G. V. 1979, *Astr. Ap.*, **75**, 351.
Norris, R. P., Diamond, P. J., and Booth, R. S. 1982, *Nature*, **299**, 131.
Olnon, F. M. 1977, Ph.D. thesis, University of Leiden.
Olofsson, H., Johansson, L. E. B., Hjalmarson, Å, and N-Q-Rieu 1982, *Astr. Ap.*, **107**, 128.
Reid, M. J., Moran, J. M., and Johnston, K. J. 1981, *A.J.*, **86**, 897.
Reid, M. J., Moran, J. M., Leach, R. W., Ball, J. A., Johnston, K. J., Spencer, J. H., and Swenson, G. W. 1979, *Ap. J. (Letters)*, **227**, L89.
Reid, M. J., and Muhleman, D. O. 1978, *Ap. J.*, **220**, 229.
Reid, M. J., Muhleman, D. O., Moran, J. M., Johnston, K. J., and Schwartz, P. R. 1977, *Ap. J.*, **214**, 60.
Rosen, B. R., Moran, J. M., Reid, M. J., Walker, R. C., Burke, B. F., Johnston, K. J., and Spencer, J. H. 1978, *Ap. J.*, **222**, 132.
Scalo, J. M., and Slavsky, D. B. 1980, *Ap. J. (Letters)*, **239**, L73.
Schmidt, G. D., Angel, J. R. P., and Beaver, E. A. 1978, *Ap. J.*, **219**, 477.
Spencer, J. H., Bowers, P. F., and Johnston, K. J. 1983, *Ap. J.*, submitted (SBJ).
van Blerkom, D. 1978, *Ap. J.*, **223**, 835.
Werner, M. W., Beckwith, S., Gatley, I., Sellgren, K., Berriman, G., and Whiting, D. L. 1980, *Ap. J.*, **239**, 540.
Wolff, R. S., and Carlson, E. R. 1982, *Ap. J.*, **257**, 161.
Zuckerman, B. 1980, *Ann. Rev. Astr. Ap.*, **18**, 263.
Zuckerman, B., Gilra, D., Turner, B. E., Morris, M., and Palmer, P. 1976, *Ap. J. (Letters)*, **205**, L15.
Zuckerman, B., Palmer, P., Gilra, D., Turner, B. E., and Morris, M. 1978, *Ap. J. (Letters)*, **220**, L53.
Zuckerman, B., Palmer, P., Morris, M., Turner, B. E., Gilra, D. P., Bowers P. F., and Gilmore, W. 1977, *Ap. J. (Letters)*, **211**, L97.

P. F. BOWERS, K. J. JOHNSTON, and J. H. SPENCER: Code 4130, Naval Research Laboratory, Washington, DC 20375